

Advances in Analysis of Low Signal-to-Noise Images Link Dynamin and AP2 to the Functions of an Endocytic Checkpoint

François Aguet,¹ Costin N. Antonescu,^{2,3,4} Marcel Mettlen,^{2,3,5} Sandra L. Schmid,^{2,5,*} and Gaudenz Danuser^{1,*}

¹Department of Cell Biology, Harvard Medical School, Boston, MA 02115, USA

²Department of Cell Biology, The Scripps Research Institute, La Jolla, CA 92037, USA

³These authors contributed equally to this work

⁴Present address: Department of Chemistry and Biology, Ryerson University, Toronto, ON M5B 2K3, Canada

⁵Present address: Department of Cell Biology, University of Texas Southwestern Medical Center, Dallas, TX 75390, USA

*Correspondence: sandra.schmid@utsouthwestern.edu (S.L.S.), gaudenz_danuser@hms.harvard.edu (G.D.)

<http://dx.doi.org/10.1016/j.devcel.2013.06.019>

SUMMARY

Numerous endocytic accessory proteins (EAPs) mediate assembly and maturation of clathrin-coated pits (CCPs) into cargo-containing vesicles. Analysis of EAP function through bulk measurement of cargo uptake has been hampered due to potential redundancy among EAPs and, as we show here, the plasticity and resilience of clathrin-mediated endocytosis (CME). Instead, EAP function is best studied by uncovering the correlation between variations in EAP association to individual CCPs and the resulting variations in maturation. However, most EAPs bind to CCPs in low numbers, making the measurement of EAP association via fused fluorescent reporters highly susceptible to detection errors. Here, we present a framework for unbiased measurement of EAP recruitment to CCPs and their direct effects on CCP dynamics. We identify dynamin and the EAP-binding α -adaptin appendage domain of the AP2 adaptor as switches in a regulated, multistep maturation process and provide direct evidence for a molecular checkpoint in CME.

INTRODUCTION

Clathrin-mediated endocytosis (CME) is a major pathway for internalizing cell surface proteins and receptors (Ferguson and De Camilli, 2012; McMahon and Boucrot, 2011; Traub, 2009). During this process, clathrin and the adaptor protein AP2 assemble into clathrin-coated pits (CCPs) on the plasma membrane, which invaginate and mature with the help of other endocytic accessory proteins (EAPs) (McMahon and Boucrot, 2011). Upon maturation, the GTPase dynamin catalyzes membrane scission, leading to the formation of cargo-containing vesicles.

Live-cell imaging studies have revealed a remarkable heterogeneity in CCP assembly kinetics within individual mammalian cells (Ehrlich et al., 2004; Loerke et al., 2009; Merrifield et al., 2002; Rappoport et al., 2003; Taylor et al., 2011), with CCP life-

time analysis revealing two short-lived “abortive” subpopulations and a longer-lived “productive” subpopulation (Ehrlich et al., 2004; Loerke et al., 2009). Experimental manipulation of cargo concentration (Loerke et al., 2009) and clustering (Liu et al., 2010), as well as small interfering RNA (siRNA) knockdown of a subset of EAPs (Mettlen et al., 2009b), shifted the relative proportions of the three subpopulations, suggesting that transitions between them could be gated by molecular checkpoints monitoring the state of assembly, cargo recruitment, and potentially other physical properties of CCPs, such as curvature. However, whether these checkpoints are the consequence of a purely stochastic process or part of an active control mechanism that monitors CCP maturation remains unknown. In this regard, evidence suggests that dynamin may be involved in regulating CCP maturation in addition to its function in vesicle scission (Loerke et al., 2009; Mettlen et al., 2009a; Sever et al., 2000), although its early role in CME remains controversial (Doyon et al., 2011; Ferguson and De Camilli, 2012; McMahon and Boucrot, 2011).

An extensive network of EAPs has been characterized (Schmid and McMahon, 2007; Taylor et al., 2011), but how these factors contribute to the regulation of CCP maturation and whether they function through a putative checkpoint mechanism is unclear, in part because perturbation of EAPs does not yield an unambiguous phenotype. Indeed, siRNA knockdown studies of individual EAPs generally produce only mild effects on the efficiency of transferrin (Tfn) internalization by CME (Huang et al., 2004). Moreover, despite the fact that many EAPs interact through short peptide motifs with the AP2 α -adaptin appendage domain, siRNA knockdown and reconstitution studies demonstrated that Tfn uptake was fully supported by a truncated α -adaptin lacking this domain (Motley et al., 2006). These studies suggested that redundancy precludes diagnosis of EAP function through bulk measurement of CME efficiency. A potentially more sensitive approach to dissect EAP function is to examine the effect of their association on the dynamics and lifetimes of individual CCPs (Henry et al., 2012; Mettlen et al., 2009b).

CCP lifetimes are measured in time-lapse images of cells expressing fluorescently labeled subunits of clathrin or AP2, using spinning disk confocal or total internal reflection fluorescence microscopy (TIRFM). CCPs, generally smaller than 200 nm in diameter, generate a diffraction-limited fluorescence signal

that can be detected and tracked using particle tracking software. Several factors affect the accuracy of the resulting lifetimes: (1) the expression level of the fluorescent reporter, which largely determines the signal-to-noise ratio (SNR); (2) the sensitivity and selectivity of the detection method used to identify CCPs; (3) the capability of the tracking method to interpolate missing information when CCP fluorescence is not detected; (4) the choice of fiducial protein, e.g., clathrin or AP2, and potential perturbation effects of the fluorescent tag; and (5) the susceptibility of the fluorophore to bleaching, which constrains exposure time and excitation intensity.

In the past, labeling has been achieved by overexpressing a fluorescent fusion of clathrin light chain a (CLCa) or of one of the AP2 subunits. Both approaches preserve the stoichiometry of clathrin triskelions and adaptors and have been shown to preserve CME function and dynamics (Ehrlich et al., 2004; Gaidarov et al., 1999; Loerke et al., 2009). However, using genome-edited cells expressing CLCa-red fluorescent protein (RFP) from the endogenous locus, Doyon et al. (2011) reported CCP lifetimes that were approximately half of those measured in cells overexpressing enhanced green fluorescent protein (EGFP)-CLCa. While this result raised the concern that much of the imaging data relying on overexpressed fusion constructs could be invalid, the significantly lower fluorescence signal for endogenously expressed CLCa-RFP versus overexpressed EGFP-CLCa also presents enormous challenges that could prevent accurate acquisition of complete CCP traces.

Here, we report the development and validation of highly sensitive and quantitative imaging approaches to acquire and classify complete CCP trajectories and then use these tools to resolve discrepancies regarding the effects of CLCa overexpression, early dynamin function, and the role of AP2-EAP interactions.

RESULTS

Overexpressed Fluorescent Fusions of Clathrin Light Chain Do Not Inhibit CME

Clathrin is the most abundant CCP protein. Thus, labeled clathrin light chains (CLCs) are optimal markers to follow the dynamics of CME in living cells (Ehrlich et al., 2004; Gaidarov et al., 1999; Loerke et al., 2009). CLCa and CLCb bind interchangeably, yet substoichiometrically (Girard et al., 2005), to clathrin heavy chain (CHC) trimers to form clathrin triskelions. In cell lines overexpressing a fluorescent fusion of CLCa (i.e., EGFP-CLCa), unincorporated CLCs are degraded; thus, endogenous CLCs are downregulated (Figure S1A available online). Hence, the fusion protein effectively outcompetes the endogenous, unlabeled CLCa/b and saturates binding to CHC (Figures S1A–S1C). In contrast, endogenously tagged CLCa-RFP (enCLCa-RFP) is substoichiometrically incorporated (Cocucci et al., 2012), leaving a significant portion of the triskelia without fluorescence and generating much weaker signals for tracking CCPs.

To resolve the discrepancy in CME dynamics observed between cells overexpressing EGFP-CLCa fusions (EGFP-CLCa O/X cells) and genome-edited cells expressing endogenous levels of CLC-RFP (enCLCa-RFP cells), we first replicated earlier control experiments that had shown no measurable effect on Tfn uptake in CLC-overexpressing cells. Contrary to the report of Doyon et al. (2011), we observed no inhibition of

Tfn uptake at either low or high levels of adenovirus-mediated overexpression of CLCa or CLCb (Figure S1D), regardless of whether we used N- or C-terminal fusions (Figure S1E) or genes from different species (rat or monkey; Figure S1F). These results confirmed that overexpressed fluorescent CLC fusions do not functionally perturb CME.

Automated Detection of CCPs in Live-Cell Images by TIRFM

One explanation for the reduced lifetimes of CCPs measured in enCLCa-RFP cells is the difficulty in accurately tracking CCP trajectories at lower SNRs. To generate unbiased CCP lifetime distributions at low SNR, we developed a computational analysis framework for the detection of image signals from clathrin-coated structures (CCSs) and compared CCS lifetimes extracted from total internal reflection fluorescence (TIRF) movies of EGFP-CLCa O/X cells with those of cells expressing enCLCa-RFP. Images were acquired at 1 frame \times s⁻¹ for 10 min, with illumination conditions chosen to maximize CCS fluorescence with minimal bleaching (see Supplemental Experimental Procedures); the imaging conditions used for enCLCa-RFP cells matched those described in Doyon et al. (2011). Performance analysis on a previously used wavelet-based detection algorithm (Loerke et al., 2009) suggested a significant fraction of false-positive and missed detections, both at the SNR achievable in EGFP-CLCa O/X cells and the lower SNR obtained in enCLCa-RFP cells (Figure 1A). By design, wavelets place relatively weak constraints on the shape and size of the detected objects and the distinction of true- from false-positives requires the use of arbitrary thresholds. In the case of diffraction-limited CCSs, much stronger constraints can be imposed through a model-based detection of signals with the characteristics of a point spread function (PSF). Moreover, model-based approaches allow the computation of uncertainty in the model parameters, which enables selection of valid CCS signals based on unbiased statistical tests. We modeled CCS fluorescence as a two-dimensional Gaussian approximation of the microscope PSF (Cheezum et al., 2001) above a spatially varying local background (see Supplemental Experimental Procedures). The actual detection algorithm encompasses two steps: a filter to identify pixels likely to contain CCS fluorescence and a subsequent model-fitting step performing subpixel localization at each putative CCS position (Figure S2A; Supplemental Experimental Procedures). We used the residuals of the model fit to calculate, for each candidate CCS signal, the uncertainty and statistical significance of the estimated fluorescence amplitude. Among these candidates, signals were selected as valid CCS detections if the amplitude was above a 95th percentile confidence threshold in the local background noise distribution calculated from the residuals (Figures S2B and S2C; Supplemental Experimental Procedures). This approach significantly improves detection sensitivity and selectivity compared to prior approaches developed for particle tracking and super-resolution microscopy (which usually rely on hard thresholds on amplitude-to-background ratio for signal selection; Figure S2D) and resulted in reliable detection of CCS fluorescence in either EGFP-CLCa O/X or enCLCa-RFP cells (Figure 1A; Movies S1 and S2).

To obtain complete fluorescence trajectories of the detected CCSs, we used tracking software to link corresponding locations

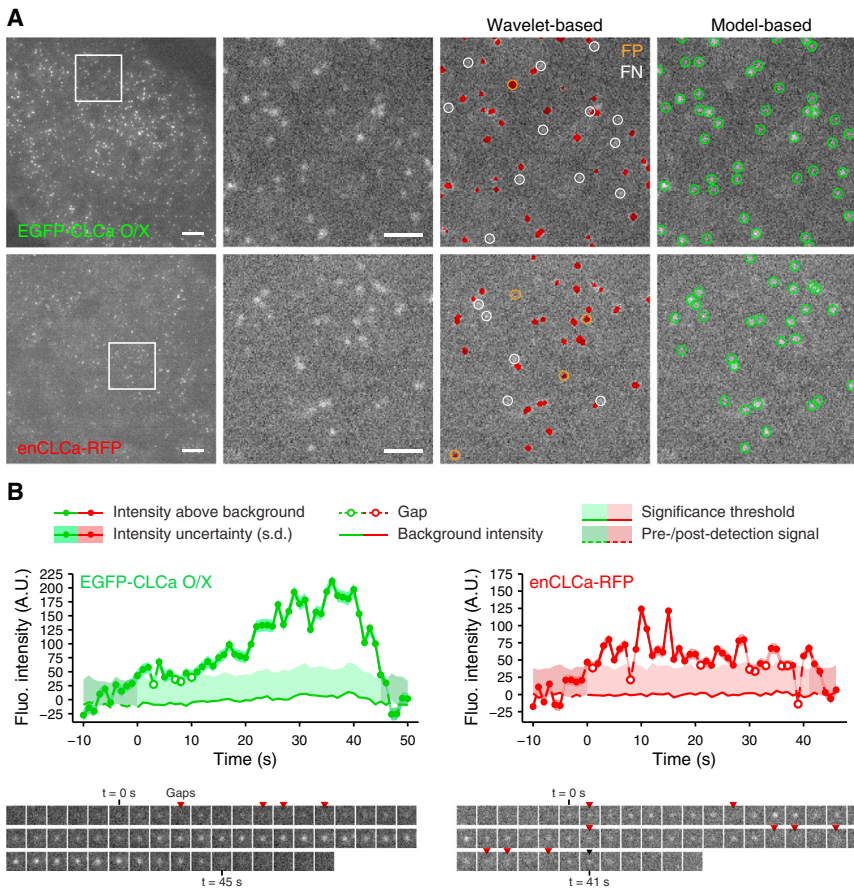


Figure 1. Model-Based Detection of CCSs

(A) Detection of CCSs in BSC1 cells over-expressing EGFP-CLCa (EGFP-CLCa O/X, top row) or expressing genome-edited, endogenous CLCa-RFP (enCLCa-RFP, bottom row), imaged by TIRFM. Red patches indicate pixels detected as significant by a wavelet-based detection (Loerke et al., 2009); green circles indicate positions of CCSs detected with the model-based algorithm proposed here (see Supplemental Experimental Procedures). False-positives (FP) and false-negatives (FN) of the wavelet-based detection are in reference to the model-based detections. Scale bars: 5 μ m, first column, and 2 μ m, magnified insets.

(B) Representative intensity traces of CCSs identified by model-based detection and tracking of EGFP-CLCa O/X and enCLCa-RFP. Gaps are defined as frames missed by the detection but recovered during tracking. Uncertainties for the detected intensities (shown as SD, dark shaded band) and the significance threshold (~ 2 SD above background noise, light shaded area) were estimated using the residuals from the model fit to the raw image signal (see Supplemental Experimental Procedures). Residual signals in the dark shaded regions preceding and following the first and last detected CCS signals, respectively, were measured to verify detection of independent events (see Supplemental Experimental Procedures). Shown below are individual frames of each trace.

See also Figures S1 and S2 and Movies S1 and S2.

between consecutive frames as well as to fill in missing detections, or “gaps” (Jaqaman et al., 2008). The latter is critical when the CCS signal fluctuates about the detection limit, as is frequently the case during CCS assembly (Figure 1B). In EGFP-CLCa O/X cells, the traces thus obtained displayed increasing intensity, reflecting CCP growth and maturation (Figure 1B, left panel), whereas in enCLCa-RFP cells, intensity traces were significantly corrupted by noise and often barely persisted above the detection threshold (Figure 1B, right panel).

Robust Measurement of CCP Lifetime Distributions

Equipped with this detection algorithm, we first determined the lifetime distributions of all detected clathrin structures (CSs) in EGFP-CLCa O/X cells (Figure 2A). Relative to previous studies using simpler image processing methods (Ehrlich et al., 2004; Loerke et al., 2009), we detected many more short-lived CSs that emitted very low levels of fluorescence (Figure 2B). Half of the detected events had a lifetime < 20 s (Figure 2B, inset). We suspect that these events correspond to the stochastic and transient assembly of small coat fragments. To identify and measure the lifetime distributions of bona fide CCPs, i.e., those undergoing a stabilization and maturation process, we established objective and quantitative criteria to filter out the predominant contribution of these transient CSs.

The robust measurement of CCS lifetime distributions generally requires the pooling of measurements from multiple cells (Loerke et al., 2009). Therefore, we first needed to account for

variations in the EGFP-CLCa expression level between cells. To this end, we applied an intensity normalization based on the per-cell distributions of the maximum fluorescence emitted by each CCP (Figure 2C, top panel). Scaling each distribution linearly to the median distribution yielded a remarkable overlap between the corrected distributions (Figure 2C, bottom panel; Supplemental Experimental Procedures). The scaling values varied between ~ 0.9 and 1.1 , clearly within the expected variations in EGFP-CLCa expression. Thus, apart from expression level variation, CCP populations follow a stereotypical range of CLCa incorporation.

Next, we grouped CSs into cohorts with a specific range of lifetimes and generated an intensity distribution for each of the first ten detected time points over the CS population in a cohort (Figure 2D). The first detected time point of each CS, regardless of cohort, occurs at the same intensity level (narrow distribution at time 0; Figure 2D), i.e., upon accumulation of the same number of EGFP-CLCa. Subsequently, due to heterogeneity in the CS assembly process, the distributions broaden. Starting at 1 s, they include intensities that are below the detection threshold of the first frame, which were recovered by gap closing during tracking. This representation shows that, regardless of lifetime, the median rate of EGFP-CLCa incorporation during the first ~ 6 s is identical for all detected structures (Figure 2D). The fluorescence intensity of a majority of CSs in the shortest lifetime cohorts (< 10 s and 10–15 s) never exceeded the level reached during this initial phase of assembly (Figure 2E; cf. first 6 s

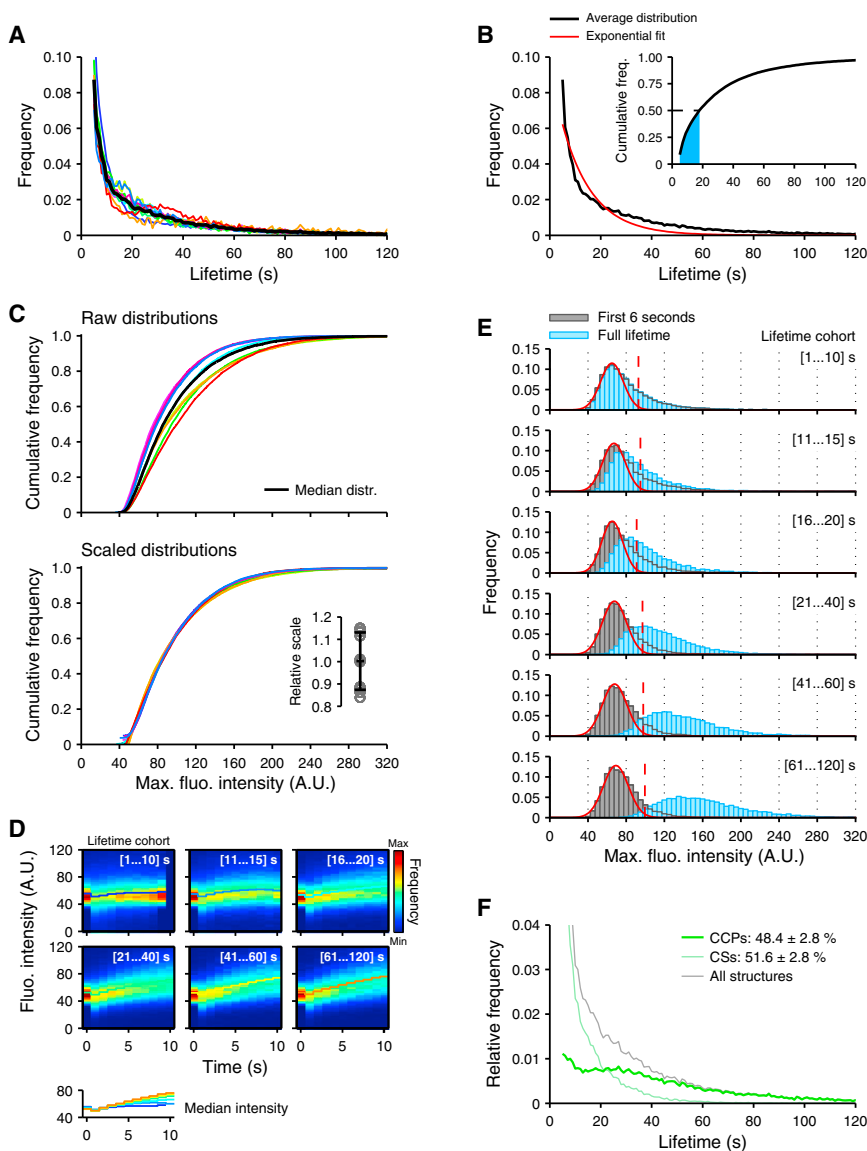


Figure 2. Intensity-Based Thresholding of Trajectories to Identify Bona Fide CCPs

(A) Lifetime distribution of detected CCSs from ten cells overexpressing EGFP-CLCa (colored traces, individual cells; black trace, population average); $\sim 9,000 \pm 3,000$ CCSs per cell.

(B) Result of the best exponential fit (red) to the average distribution (black; from A). Inset, cumulative distribution. Fifty percent of CCSs have a lifetime < 20 s.

(C) Colored traces (top) show cumulative distributions of maximum fluorescence intensity over the lifetime of a CCS in individual cells; black trace, median distribution. After linear scaling (bottom; see Supplemental Experimental Procedures), the distributions narrowly overlay, indicating that the CCS maximum intensity distribution is invariant across cells. Inset, distribution of the scaling factors (mean \pm SD, 0.99 ± 0.13).

(D) CCS fluorescence (Fluo.) intensity versus time for different lifetime cohorts. Distributions were calculated from CCSs of ten cells and normalized for each of the ten first time points in the life of a CCS. The median intensity (lower panel) is lifetime invariant during the first ~ 6 s of assembly. a.u., arbitrary units.

(E) Maximum intensity distributions from scaled CCS intensity traces for different lifetime cohorts. Gray histograms indicate distribution of maximum intensities reached during the first 6 s of a CCS trace. Blue histograms indicate distribution of maximum intensities reached over the full lifetime of a CCS trace. Overlaid red curves indicate best fitting Gaussian distributions to the first mode of the 6 s histograms; dashed lines indicate the 95th percentile of these distributions, which served as a threshold to classify CCSs into transient assemblies (maximum intensity remains below threshold) or bona fide CCPs undergoing maturation (maximum intensity surpasses threshold).

(F) Average lifetime distribution for bona fide CCPs and transient assemblies (CSs) resulting from application of the threshold.

[gray histograms] with total distribution [blue histograms]). In contrast, for longer-lived cohorts, especially those representing CSs with lifetimes > 20 s, the intensity distributions beyond 6 s display a systematic increase, indicating the successful nucleation and growth of a nascent CCP. The intensity level of CSs at times < 6 s thus provided a threshold for the partitioning of CSs into transient coat fragments versus CCPs that enter a maturation process. To obtain a robust estimate of the threshold, we calculated the Gaussian function best fitting the first peak in the distribution of maximum fluorescence intensities reached in the first 6 s of CS age, across all lifetime cohorts (Figure 2E, red curve; Supplemental Experimental Procedures). The threshold was selected as the 95th percentile of the fitted Gaussian. CSs were then partitioned into two groups: those for which fluorescence intensity exceeds the intensity threshold at any time of the CS trace and those for which fluorescence maximum remains below the threshold. The two populations were of approximately equal size yet had distinct lifetime distributions

(Figure 2F). For the population of CSs below the threshold, the distribution showed a rapid, quasi-exponentially decaying process, characteristic of the stochastic disassembly of labile coat structures (Figure S3A), with a mean lifetime of ~ 14 s. The population of above-threshold, maturing CCPs included all events with a lifetime greater than ~ 40 s. The maximal intensities of traces in this group varied widely, confirming that the CCP maturation process generates a broad range of coat sizes. Within this population, an anomalous peak of short-lived events (< 15 s) remained. We speculated that this population might include events associated with the transient appearance of intracellular membranes coated with clathrin (e.g., originating from endosomes or Golgi, hereinafter termed “visitors”) in the TIRF illumination field. Hence, it was necessary to develop an additional filter that would remove such CME-unrelated signals.

A comparison of the average above-threshold intensities of lifetime cohorts in the CCP population showed that short lifetime cohorts (10–19 s and 20–29 s) included structures that grew at a

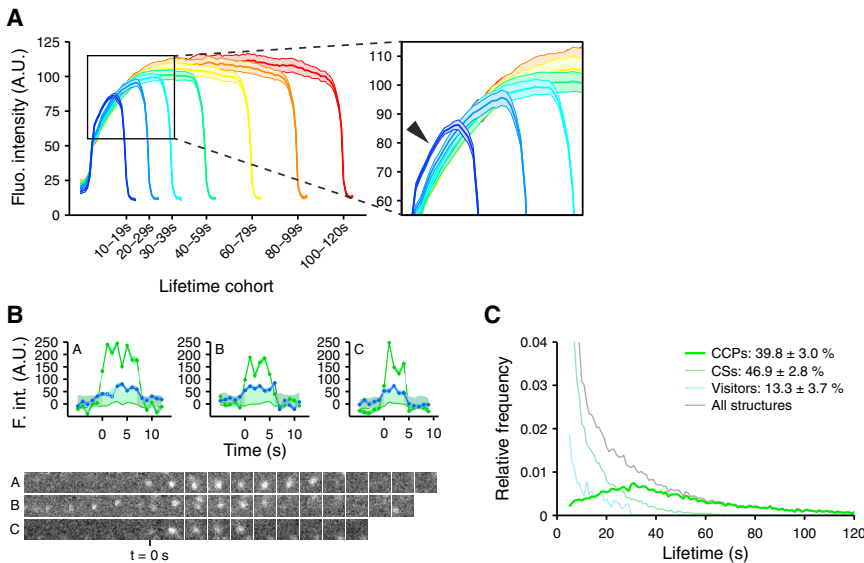


Figure 3. Exclusion of Short-Lived, Instantaneously Appearing CCSs

(A) Averaged CCS intensity traces per lifetime cohort, shown as mean \pm SE (shaded areas) for all above-threshold CCSs. Inset, enlarged scale showing aberrant rapid rise in intensity of short-lived (<20 s) CCSs (arrowhead).

(B) Examples of intensity traces (green) with instantaneous appearance at an acquisition rate of 1 frame s^{-1} . The majority lasts for less than 10 s, and intensity prior to the first detected frame is at background level, in contrast to CCPs of equally short lifetime (blue).

(C) Subtraction of subthreshold (light green) and transient (light blue) CCSs from all detected CCSs (gray) yields an average lifetime distribution for bona fide CCPs that reflects a multistep maturation process.

See also Figure S3.

significantly faster rate than that observed in longer-lived cohorts (Figure 3A). Consistent with the notion that visitors enter the TIRF illumination field as complete assemblies, inspection of the fast-growing events revealed that a majority corresponded to the quasi-instantaneous appearance of a strong signal (Figure 3B). For these events, the intensity in the frames prior to the first detection were at the background level, in contrast to assembling CCPs, which showed a gradual increase in intensity (Figure 3B, blue traces; see also Figure 1B). Exclusion of visitors based on these characteristics eliminated a large fraction of short-lived events from the CCP population. Henceforth, we simply refer to the remaining population of bona fide CCPs as “CCPs.” Their lifetime distribution was characteristic of a process governed by the superposition of multiple steps (Figures 3C and S3B), which may include nucleation, stabilization, maturation, and internalization.

Accurate Measurement of CCP Lifetimes Requires High SNR Missed by Endogenous Labels

When applied to EGFP-CLCa O/X and enCLCa-RFP cells, our framework confirmed the previous report (Doyon et al., 2011) in that the lifetimes of CCPs measured with enCLCa-RFP were significantly shorter than those measured with EGFP-CLCa O/X (Figure 4A). Moreover, even after rejection of $\sim 47\%$ of detected CSs as coat fragments, the lifetime distributions in enCLCa-RFP cells still exhibited a quasi-exponential decay. These fundamental differences in CCP lifetime behavior could be related to the difference in CLCa expression levels between the cell types, as suggested by (Doyon et al., 2011), and/or an artificial fragmentation of tracks in enCLCa-RFP cells associated with an increased number of prolonged detection misses due to much lower image SNR (Figure 4A, inset). Indeed, simulations showed that a lifetime distribution corresponding to CCPs in EGFP-CLCa O/X cells could be transformed into a quasi-exponentially decaying distribution by as few as one uncompensated gap per track or by gaps occurring with a probability experimentally derived from the analysis of EGFP-CLCa O/X cells (Figure 4B; see Supplemental Experimental Procedures for a

discussion of gap-closing accuracy). Thus, we conjectured that much of the apparent CCP lifetime reduction in enCLCa-RFP cells compared to EGFP-CLCa O/X cells is related to detection misses that remained unidentified by our gap-closing algorithm.

To test this, we expressed in enCLCa-RFP cells an internal EGFP fusion to the $\mu 2$ subunit ($\mu 2$ -EGFP) of AP2 as a second marker of CCPs (Huang et al., 2003). Similar to CLCa, overexpression of $\mu 2$ -EGFP outcompetes the endogenous subunit and does not modify the concentration of AP2 or the rate of CME (Ehrlich et al., 2004). We then performed two separate analyses of EGFP/RFP image time-lapse sequences. First, we tracked CCPs in the $\mu 2$ -EGFP channel (“ $\mu 2$ -EGFP master”) in order to capture complete CCP trajectories, and we measured the associated fluorescence intensity in the enCLCa-RFP channel (“enCLCa-RFP slave”; Figure 4C; Supplemental Experimental Procedures). Next, we tracked CCPs in the enCLCa-RFP channel alone (“enCLCa-RFP master”) and compared the trajectories to those tracked by $\mu 2$ -EGFP (Movie S3). Due to the transient expression of $\mu 2$ -EGFP in these experiments, the replacement of endogenous with the tagged version of this subunit was nonsaturating, so that some CCPs had undetectable levels of $\mu 2$ -EGFP fluorescence. Similarly, due to the low level of enCLCa-RFP relative to unlabeled CLC in these cells (Figure S1C), enCLCa-RFP could not be detected in a fraction of CCPs with detectable $\mu 2$ -EGFP. To restrict our comparisons to CCP trajectories that were detected in both master channels, we calculated a mutual mapping of the trajectories identified by the two analyses (see Supplemental Experimental Procedures). As hypothesized, the CCP lifetime distribution measured by enCLCa-RFP was skewed toward significantly shorter values, compared with the distribution of the same CCPs measured by $\mu 2$ -EGFP (Figure 4D). On average, measurements obtained by enCLCa-RFP resulted in an underestimation of lifetimes by a factor of ~ 1.8 (Figure 4E), which was consistent with the discrepancy reported by Doyon et al. (2011). Moreover, the mean values of the $\mu 2$ -EGFP and EGFP-CLCa O/X distributions were indistinguishable within the limits of experimental uncertainty, indicating

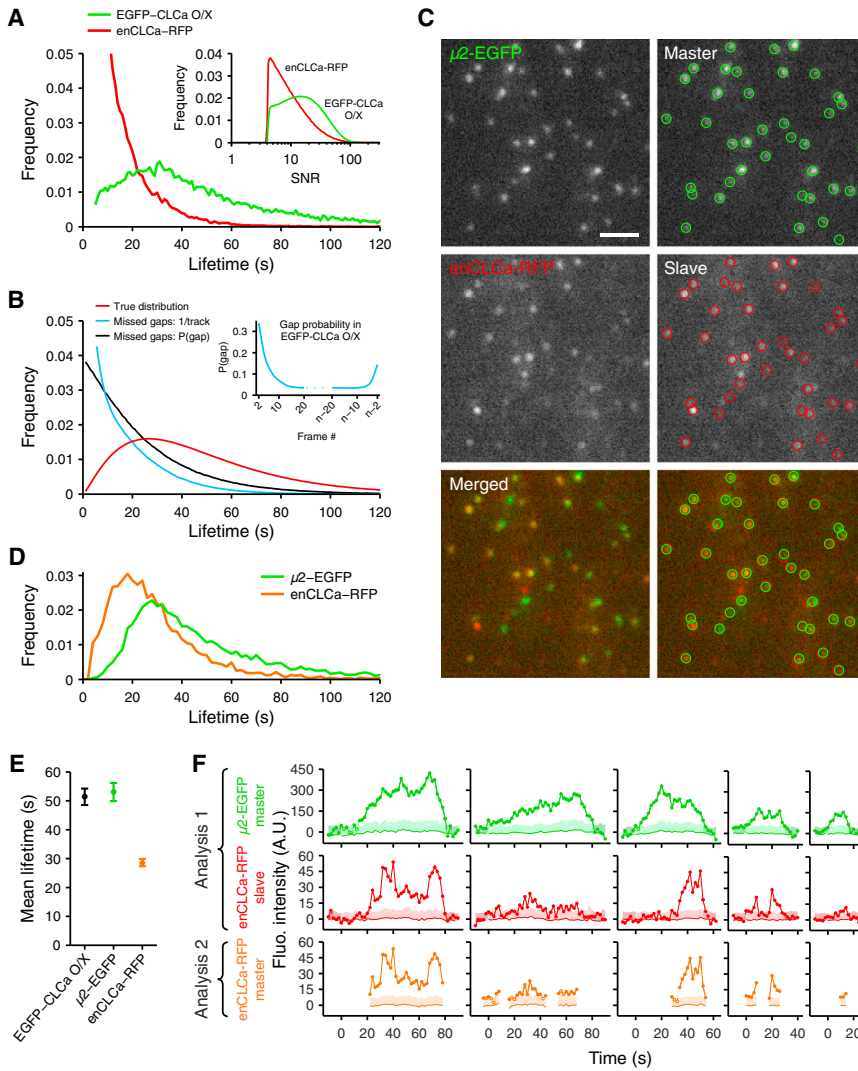


Figure 4. SNR Achieved with Endogenous Levels of Fluorescently Labeled CLCa Is Insufficient for Accurate Lifetime Measurements

(A) Average lifetime distributions of CCPs for cells overexpressing EGFP-CLCa (green, same data as in Figure 3) and for genome-edited enCLCa-RFP cells (red, average of nine cells). Inset, distribution of SNR for all CCP detections in enCLCa-RFP and EGFP-CLCa O/X cells.

(B) Simulation demonstrating the effects on lifetime distribution of missed detections (gaps) or insufficient gap closing during tracking. Red curve indicates reference gamma distribution fitted to EGFP-CLCa O/X lifetimes in (A) (rate parameter $k = 0.05 \text{ s}^{-1}$; shape parameter $n = 2.3$). Introduction of a single gap with uniform probability, or gap(s) based on the probability of occurrence derived from the EGFP-CLCa O/X data (inset), produces a quasi-exponential lifetime distribution (black and blue lines, respectively, simulated from 10^6 trajectories).

(C) Master/slave detection of CCPs in genome-edited enCLCa-RFP cells overexpressing $\mu 2$ -EGFP. Detection was performed on the $\mu 2$ -EGFP “master” channel (first column); fluorescence intensities in the enCLCa-RFP “slave” channel were estimated by subpixel localization at the detected $\mu 2$ -EGFP positions (second column; see Supplemental Experimental Procedures). Scale bar, $2 \mu\text{m}$.

(D) Lifetime distributions of CCPs measured independently using either the $\mu 2$ -EGFP or the enCLCa-RFP channel. The enCLCa-RFP distribution was calculated from enCLCa-RFP trajectories with an associated $\mu 2$ -EGFP signal and vice versa (see Supplemental Experimental Procedures).

(E) Mean CCP lifetimes in EGFP-LCa O/X cells (black) and in enCLCa-RFP cells using the overexpressed $\mu 2$ -EGFP marker (green) or using enCLCa-RFP (orange). Error bars: cell-to-cell variation, shown as SD from nine cells or more per condition.

(F) Example intensity traces obtained by tracking either $\mu 2$ -EGFP detections (analysis 1, shown with the associated enCLCa-RFP “slave” signal), or enCLCa-RFP detections (analysis 2). See also Movie S3.

that these two markers are equivalent reporters of CCP dynamics (Figure 4E). Mapping of trajectories from the two analyses allowed us to identify time-shifted fragments that belonged to the same CCP (e.g., second column of panels in Figure 4F). Foremost, this mapping shows that the apparent shorter lifetimes measured by enCLCa-RFP effectively resulted from truncation and/or fragmentation of trajectories, particularly during early time points when the clathrin coat still consists of few triskelia (e.g., Figure 4F, third and fourth columns). Hence, these data demonstrate that the previously reported shorter and more homogeneous lifetimes of CCPs in stable enCLCa-RFP cells versus EGFP-CLCa O/X cells are not the result of perturbations in CCP maturation. Rather, they highlight the critical influence of SNR on lifetime measurements and the need for validation of lifetime distributions by the use of overexpressed, fluorescently tagged CLCa or AP2 subunits as robust fiducial markers of CCPs.

Sensitive Detection of Endogenously Labeled Dynamin-2 Reveals an Early Recruitment and Function for Dynamin in CME

We next applied this analysis to resolve controversies regarding the temporal hierarchy of dynamin recruitment to CCPs. The GTPase dynamin is generally associated with late stages of CME in mammalian cells, where it assembles into collar-like structures around the necks of mature CCPs and catalyzes membrane fission to release clathrin-coated vesicles (CCVs) (Ferguson and De Camilli, 2012; Schmid and Frolov, 2011). Dynamin has also been suggested to function at earlier stages to regulate CCP maturation (Conner and Schmid, 2003; Mettlen et al., 2009a). Indirect evidence for such early roles primarily derives from expression of hypomorphic mutants that block CME at intermediate stages of CCP maturation (Damke et al., 2001), accelerate the rate of CME (Sever et al., 2000), and/or alter the lifetimes of abortive CCPs (Loerke et al., 2009). The

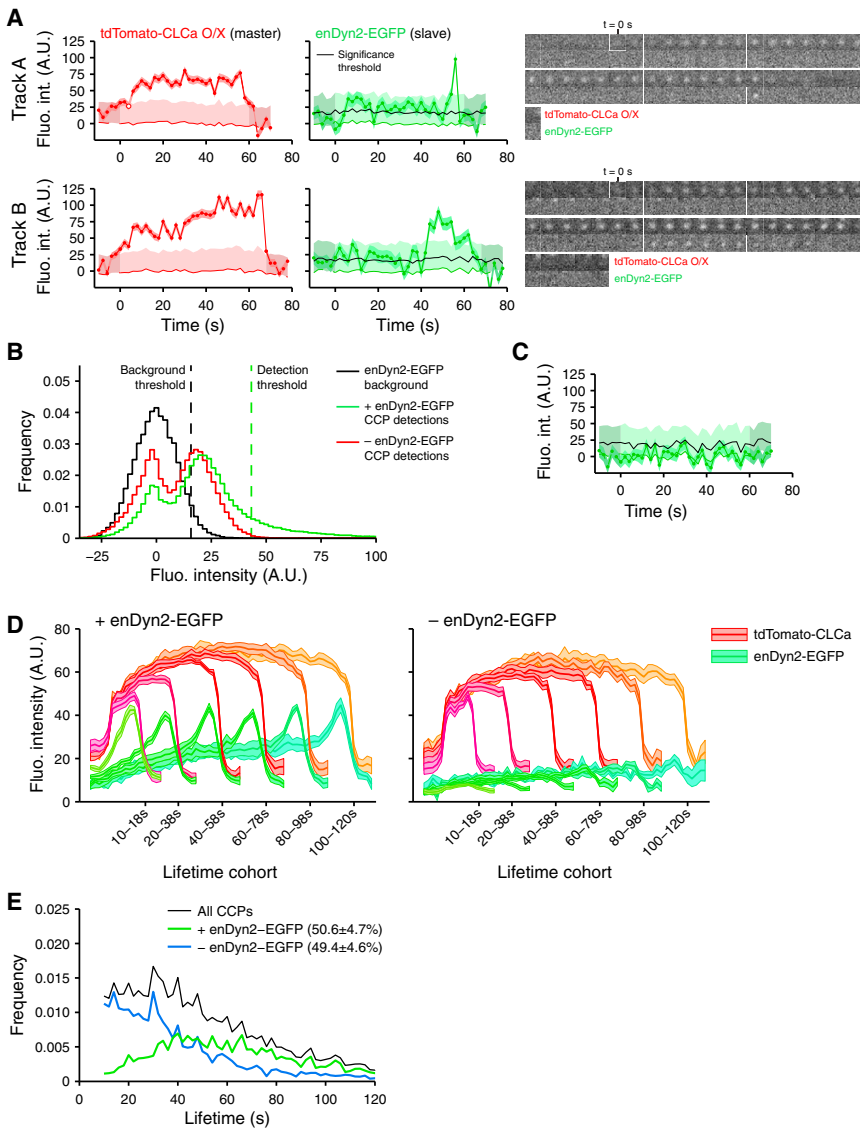


Figure 5. Dynamin Is Recruited Early in CCP Formation and Is Required for CCP Maturation via a Multistep Process

(A) Representative intensity traces of dynamin recruitment early during CCP formation followed by a characteristic peak corresponding to assembly of the scission machinery, measured in SK-MEL-2 cells expressing endogenous Dyn2-EGFP (enDyn2-EGFP) and overexpressing tdTomato-CLCa. Fluo. int., fluorescence intensity. (B) Distribution of all enDyn2-EGFP slave detections from CCPs with detectable enDyn2-EGFP fluorescence (green) and from CCPs without detectable enDyn2-EGFP (red), compared to the distribution of enDyn2-EGFP outside CCP locations (black; see [Supplemental Experimental Procedures](#)). The 95th percentile of the background distribution was selected as a threshold to identify significant enDyn2-EGFP fluorescence [black line in (A)] (see [Supplemental Experimental Procedures](#)). A CCP was Dyn2-positive when the number of time points with independently detectable enDyn2-EGFP was significantly above the expected number of such detections due to random association in a trace of equal duration (see [Supplemental Experimental Procedures](#)).

(C) Representative trace of enDyn2-EGFP intensity at a random location outside CCPs.

(D) Average clathrin (red tones) and dynamin (green tones) fluorescence intensity traces in lifetime cohorts of Dyn2-positive and Dyn2-negative CCPs (see [Supplemental Experimental Procedures](#)). Intensities are shown as mean \pm SE calculated from eight cells.

(E) Lifetime distributions of bona fide CCPs identified as described in [Figures 2 and 3](#) and further subcategorized as Dyn2-positive (green) or Dyn2-negative (blue). Characterization of enDyn2-EGFP recruitment relative to CCP disappearance and the full decomposition of lifetimes for CCPs and CSs categorized for enDyn2-EGFP recruitment are shown in [Figure S4](#). See also [Figure S4](#) and [Movie S4](#).

observation of dynamin recruitment to nascent CCPs proved more difficult because of the low abundance of labeled dynamin at CCPs, even when expression is driven by a strong ectopic promoter (Soulet et al., 2005; Taylor et al., 2011). Consequently, while some studies report early and/or transient association of dynamin with CCPs throughout their lifetimes (Ehrlich et al., 2004; Mattheyses et al., 2011; Taylor et al., 2012), using endogenously tagged dynamin-2 (enDyn2-EGFP) (Doyon et al., 2011) reported that dynamin recruitment occurred only at very late stages of CCP maturation. Moreover, because 90% of all CCPs exhibited a dynamin recruitment burst, these authors concluded that dynamin must have only minor, if any, functions in regulating CCP maturation. We wondered whether this apparent absence of endogenously labeled dynamin at early stages of CME could also be related to insufficient imaging sensitivity.

To address this, we applied master/slave detection to enDyn2-EGFP cells overexpressing tdTomato-CLCa as the

fiducial for CCPs. The tracks obtained from the tdTomato-CLCa master channel were classified as positive for dynamin if the enDyn2-EGFP signal was significant for a duration longer than random association events (see [Supplemental Experimental Procedures](#)). As previously reported (Merrifield et al., 2002), dynamin-positive CCPs tend to display a readily detectable accumulation of enDyn2-EGFP \sim 10–20 s before internalization, likely reflecting the rapid recruitment of dynamin to an assembling constriction ring ([Figure 5A](#)). However, when analyzed relative to the tdTomato-CLCa master channel, the readout of the enDyn2-EGFP signal also shows robust association shortly after CCP initiation ([Figure 5A](#); [Movie S4](#)). The tdTomato-CLCa master signal enabled the calculation of a significance threshold for enDyn2-EGFP relative to enDyn2-EGFP fluorescence outside of CCPs ([Figure 5B](#); [Supplemental Experimental Procedures](#)). Importantly, this threshold shows that, while the early enDyn2-EGFP signal is too weak for independent detection, it remains highly significant when compared against enDyn2-EGFP

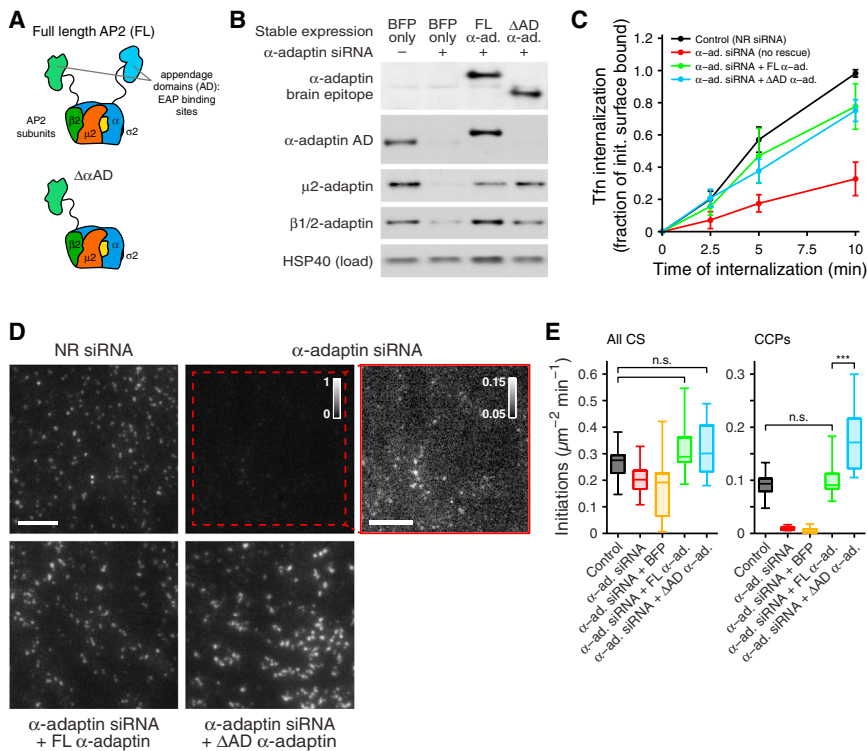


Figure 6. The AP2 α -Adaptin Appendage Domain Is Dispensable for Transferrin Uptake and CCP Initiation

(A) Schematic of the AP2 heterotetramer, showing subunits and appendage domains. The α -adaptin appendage domain (AD) has two characterized binding sites for peptide motifs present in a majority of EAPs (Praefcke et al., 2004).

(B) Immunoblots of AP-2 subunit expression. FL α -adaptin or C-terminally truncated α -adaptin lacking the appendage domain (Δ AD), each harboring siRNA-resistant mutations and bearing a brain-specific insert for detection, were stably expressed in EGFP-CLCa RPE cells. Cells expressing near-endogenous levels of each protein were selected by fluorescence-activated cell sorting, using an internal ribosome entry segment-expressed blue fluorescent protein (BFP). Cells expressing only BFP represent the control condition. The selected cells were subjected to α -adaptin siRNA to silence the endogenous protein.

(C) Tf uptake for the conditions indicated, shown as mean \pm SD of six independent experiments.

(D) EGFP-CLCa-labeled CCSs detected in fixed cells treated as indicated and imaged by TIRFM. All conditions are shown at the same dynamic range, normalized to [0..1], except for the contrast-adjusted α -adaptin siRNA comparison (rightmost panel). Scale bar, 5 μ m.

(E) Initiation density of all detected CCSs and bona fide CCPs with lifetime ≥ 5 s, for the conditions indicated (≥ 16 cells per condition). Box plots show median, 25th, and 75th percentiles, and outermost data points. ***p < 10^{-10} , permutation test.

fluorescence outside of CCPs (Figure 5C; Supplemental Experimental Procedures) or before and after formation of the clathrin coat (Figure 5A, shaded areas).

To establish that early recruitment is indeed systematic in all dynamin-positive CCPs, we averaged the enDyn2-EGFP intensity traces for a range of lifetime cohorts (Figure 5D). These averages confirm that dynamin was recruited within 20 s of initiation and accumulates at a steady rate until a rapid burst of recruitment completes the formation of the constriction ring ~ 12 s before internalization (Figure 5D). Appearance and disappearance-aligned averages of dynamin-positive CCPs show that both the average rate of recruitment during the first ~ 30 s of maturation and the average timing of the final recruitment burst relative to CCP disappearance were independent of lifetime (Figure S4A). However, at the level of individual CCPs, as previously reported (Mattheyses et al., 2011), we observed significant variation of these parameters, suggesting that the regulation of dynamin recruitment is governed by stochastic processes (Figure 5A).

Unlike the report by Doyon et al. (2011), we also identified a large fraction of dynamin-deficient CCPs ($\sim 50\%$). We compared the lifetime distributions of CCPs with or without dynamin and found significant differences both in their median lifetime (~ 65 s versus ~ 30 s) and shape (Figure 5E; for the full decomposition of lifetimes, see Figure S4B). Thus, in the absence of dynamin, the disappearance of CCPs from the plasma membrane is dramatically accelerated. More importantly, the lifetime distribution for dynamin-deficient CCPs displayed a quasi-exponential shape characteristic of a process where the disassembly of

structures is triggered by a single random event that occurs at a specific rate (Figure S3A), indicative of abortive events. In sharp contrast, the lifetime distribution of dynamin-positive CCPs peaks at ~ 40 s and then decays monotonically, indicating that the multistep processes regulating CCP assembly likely act within the first ~ 40 s of lifetime (Figures S3B and S3C). Together, these analyses establish that dynamin recruitment is a prerequisite for the formation of a productive CCP.

The AP2 α -Adaptin Appendage Domain Regulates Growth and Curvature Induction Early in CCP Assembly

Biochemical, structural, and proteomic studies have shown that the appendage domain of the α -adaptin subunit of AP2 (Figure 6A) is a central interaction hub for a majority of EAPs (Mishra et al., 2004; Motley et al., 2006; Praefcke et al., 2004) and thus should be critical for CCP formation and maturation. Contrary to this expectation, cells expressing a mutant α -adaptin lacking the appendage domain (Δ AD) and siRNA depleted of endogenous α -adaptin had no defect in Tf uptake (Motley et al., 2006). Thus, the role of AP2-EAP interactions during CCP formation has remained enigmatic, and we wondered whether our analytical approach could help resolve this discrepancy.

To replace α -adaptin at near-endogenous levels, we depleted endogenous α -adaptin by RNA interference in retrovirally transfected EGFP-CLCa retinal pigment epithelial (RPE) cells stably expressing either siRNA-resistant full-length (FL) α -adaptin or the Δ AD α -adaptin (Figure 6B). As previously reported (Motley et al., 2006), Tf uptake in siRNA-treated cells expressing the Δ AD α -adaptin (Δ AD cells) was comparable to that of untreated

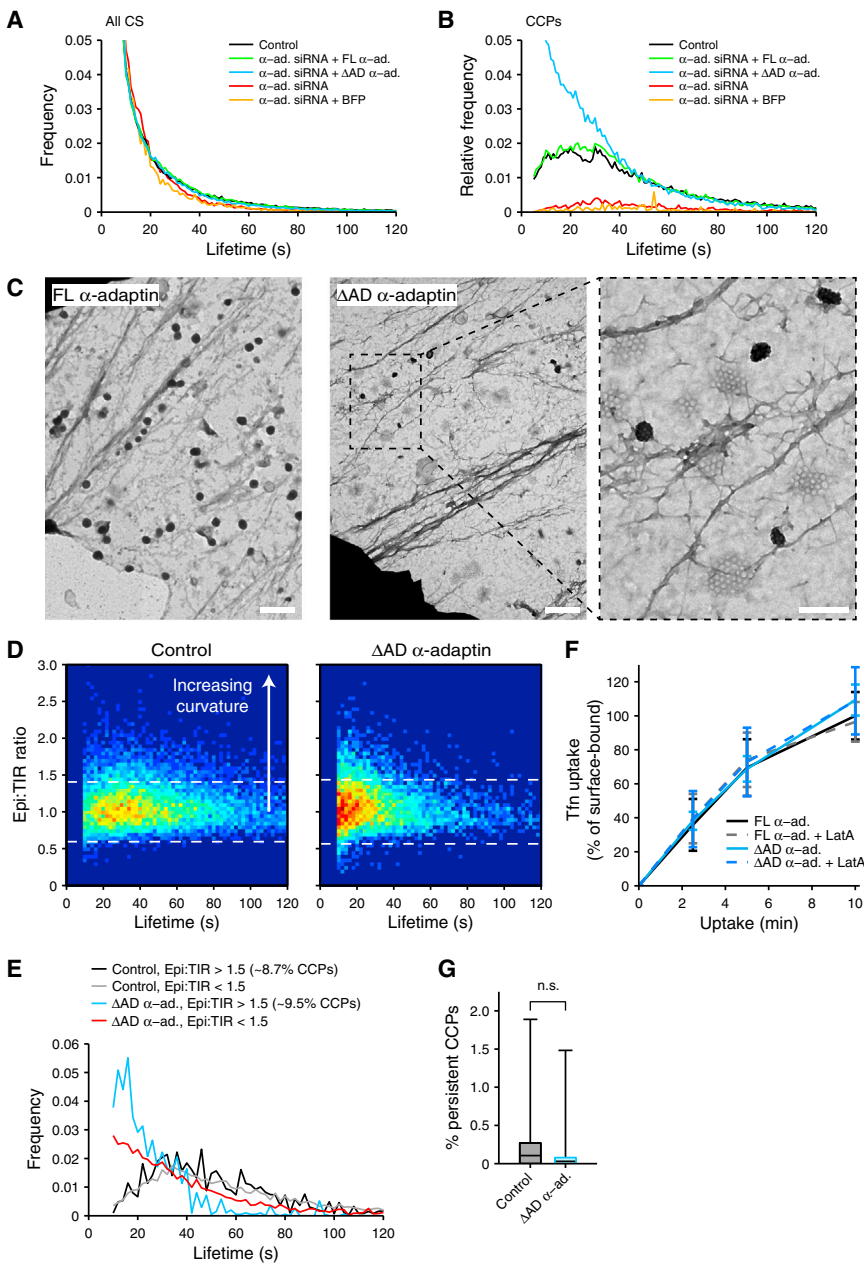


Figure 7. The AP2 α -Adaptin Appendage Domain Regulates Growth, Curvature Induction, and Maturation of Nascent CCPs

(A) Average lifetime distribution of all detected CCPs in EGFP-CLCa RPE cells for α -adaptin siRNA and re-expression conditions as indicated. (B) Average lifetime distributions of bona fide CCPs for α -adaptin siRNA and re-expression conditions as indicated.

(C) EMs of “unroofed” RPE cells expressing an siRNA-resistant FL α -adaptin or Δ AD α -adaptin construct after siRNA-mediated depletion of endogenous α -adaptin. Right panel shows higher magnification view of the indicated area. Scale bar, 500 nm; 200 nm for the magnified view.

(D) Epi:TIR ratio intensity levels for individual CCPs plotted as a function of CCP lifetime.

(E) Lifetime distributions of relatively flat (Epi:TIR ratio < 1.5) and relatively curved (Epi:TIR ratio > 1.5) CCPs in FL α -adaptin-expressing cells (control) and Δ AD α -adaptin-expressing cells.

(F) TfR internalization in cells expressing FL α -adaptin or Δ AD α -adaptin in the presence and absence of Latrunculin A (100 nM), shown as mean \pm SD of four independent experiments.

(G) Percentages of persistent CCPs, which are not included in our lifetime analysis, are not significantly different in FL α -adaptin-expressing cells versus Δ AD α -adaptin-expressing cells. Box plots show median, 25th, and 75th percentiles, and outermost data points. n.s., not significant. $p > 0.5$, permutation test.

control cells or siRNA-treated cells expressing FL α -adaptin (Figure 6C). Knockdown of endogenous α -adaptin in control cells significantly diminished CCP formation, although dim structures could still be detected (Figure 6D, upper right panels). CCP formation was retained in Δ AD cells, but they appeared brighter and more clustered than in control or FL α -adaptin cells (Figure 6D). Using our model-based detection method, we measured the rates of initiation of all detectable CSs, which were similar in all cells, even those depleted of AP2 by siRNA (Figure 6E). This result suggests that many of the low-intensity structures may correspond to AP2-independent clathrin assemblies and provides a direct validation of our filtering framework that distinguishes CCPs from coat fragments. In contrast, after filtering the data to measure only bona fide CCPs, initiations

were essentially undetectable in siRNA-treated control cells, as expected, and fully rescued by reconstitution with FL α -adaptin (Figure 6E). Unexpectedly, the rate of initiation of CCPs in Δ AD cells was approximately two times greater than in control or FL α -adaptin cells (Figure 6E).

Although the lifetime distributions for all CSs detected in control, siRNA-treated, and FL α -adaptin or Δ AD cells (Figure 7A) showed no discernable differences, we found striking differences in the lifetime distributions of bona fide CCPs (Figure 7B). In cells lacking α -adaptin, essentially no CCPs can be detected, but reconstitution with FL α -adaptin fully restored the lifetime distributions of CCPs. In contrast, a large subpopulation of CCPs that formed in Δ AD cells was short lived, with a quasi-exponentially decaying lifetime distribution. Hence, the α -adaptin appendage domain has a fundamental effect on switching CCP maturation and internalization from an unregulated random process into a regulated, multistep process (cf. Figures S3A and S3B). Most likely, this happens via recruitment of a network of EAPs that facilitate CCP maturation.

To gain further insight into the role of α -adaptin-EAP interactions in CCP maturation, we acquired electron micrographs (EMs) of the ventral surface of unroofed FL α -adaptin and Δ AD cells (Figure 7C). Although curved coated pits could be detected

in both cell populations, Δ AD cells contained a large proportion of small (<200 nm), flat, clathrin lattices rarely detected in FL α -adaptin cells. Many of these appeared in dense clusters spaced below the resolution limit of light microscopy, accounting, in part, for the apparent increase in intensity and clustering seen in fluorescence images (Figure 6D). To test whether these flat structures corresponded to the short-lived CCPs revealed by lifetime measurements, we imaged cells in dual-channel mode, alternating between TIRF and epifluorescence excitation. Because the TIR excitation field decays exponentially, the epifluorescence:TIRF intensity (Epi:TIR) ratio provides a relative measure of coat curvature. We calculated this ratio for each CCP as the maximum detected epifluorescence intensity divided by the maximum detected TIRF intensity, after calibration and adjustment of relative intensities between the two channels (see Supplemental Experimental Procedures). A peak of short-lived (<20 s) flat structures was specifically detected in Δ AD cells, presumably corresponding to the structures seen by EM. We also observed an increased number of curved pits at early time points in Δ AD cells. Hence, CCPs with high curvature seemed to mature significantly faster in Δ AD cells than in wild-type cells (Figure 7D). To examine this more closely, we calculated the 99% confidence interval about the Epi:TIR ratio of 1 expected for a flat structure (Figure 7D, dashed lines) and established 1.5 as a threshold to define highly curved structures (see Supplemental Experimental Procedures). We then calculated lifetime distributions for CCPs with an Epi:TIR ratio >1.5 and compared these to CCPs with an Epi:TIR of <1.5 (Figure 7E). This comparison revealed that, in Δ AD cells, the lifetime distribution of highly curved CCPs displays the characteristics of a multistep process with a very early maturation (peak in lifetime distribution at ~18 s; Figure 7E), while the lifetimes of less curved and flat structures follow a quasi-exponential decay. The median lifetime for curved CCPs (20 s; epi:TIR >1.5) in Δ AD cells was significantly shorter and less variable than for less curved structures (31 s; epi:TIR <1.5). In contrast, no difference was detected between the lifetime distributions of curved versus flatter structures in control cells. These data suggest that the subpopulation of productive CCPs in Δ AD cells undergo a more rapid and less regulated maturation process than those in cells expressing FL α -adaptin.

Paradoxically, Δ AD cells demonstrate a striking phenotype with regard to CCP dynamics (Figure 7B) yet do not exhibit a phenotype with regard to Tfn uptake (Figure 6C). We have identified two compensatory mechanisms in the Δ AD cells that might account, at least in part, for this discrepancy: (1) a 2-fold increase in the rate of CCP initiation that could compensate for the decrease in efficiency of nascent CCP maturation (Figure 6E); and (2) an increase in the rate of maturation of curved CCPs that could account for faster rates of Tfn uptake (Figure 7E), assuming that these highly curved structures corresponded to productive CCPs. However, a third possibility is that Tfn uptake is occurring directly from the flat lattices formed in Δ AD α -adaptin cells. Indeed, previous studies have shown that flat clathrin plaques forming on the adherent surfaces of some cell types are endocytically active and internalized in an actin-dependent manner (Saffarian et al., 2009). However, disruption of actin polymerization with latrunculin A yielded no difference in the rate of Tfn uptake between FL α -adaptin and Δ AD cells (Figure 7F),

showing that actin-mediated uptake of flat lattices is not a compensatory mechanism operating in Δ AD cells. We also compared the proportion of persistent structures in Δ AD and control cells and found no statistically significant difference (Figure 7G), indicating that the small flat lattices detected in Δ AD cells are presumably turning over in a nonproductive manner (i.e., that they represent abortive CCPs).

DISCUSSION

We developed a computational framework for sensitive and accurate detection of diffraction-limited objects and described objective criteria for the distinction of bona fide CCPs from transient clathrin assemblies detected in an evanescent field. We applied these tools to three unresolved issues regarding CCP maturation. First, we showed that the apparent lifetime differences of CCPs measured by image data tracking in cells overexpressing EGFP-CLCa versus enCLCa-RFP (Doyon et al., 2011) result only from increased detection errors at the low SNR produced by endogenous labels. Second, we provided direct evidence that dynamin-2 is recruited early during CCP formation and showed that dynamin recruitment is correlated with lifetime kinetics that are characteristic of a regulated maturation process. Third, we showed that the appendage domain of the AP2 α -adaptin subunit, through its multiple interactions with EAPs, plays critical roles at multiple stages in CME, including assembly, curvature generation, stabilization, and maturation of CCPs.

Robust Measurements of CME Dynamics

Model-based identification of diffraction-limited structures combined with refined statistical selection of significant fluorescent signals enabled us to increase the sensitivity of detection of CCPs in live cell images. Applied to endogenous CLCa-RFP and dynamin2-EGFP, we found that, despite the improved performance, the fluorescence levels measurable with endogenously tagged proteins remained too weak to be reliably and consistently detected. Importantly, we show that low signals can be detected with high sensitivity using a master/slave approach, i.e., by relying on a high-SNR reference such as overexpressed and stoichiometrically incorporated EGFP-CLCa.

EAPs compete for binding to CCP constituents through shared peptide motifs. The EAP-specific affinity for these motifs imparts hierarchy to their recruitment (Mishra et al., 2004), which is therefore particularly sensitive to overexpression. While endogenous labeling avoids such artifacts, a master/slave approach will be critical for the accurate measurement of EAP dynamics at the resulting low SNR. Approaches relying on independent detection of EAP fluorescence are prone to truncation artifacts, especially at the onset of EAP recruitment when the SNR is lowest. Such artifacts are amplified when average recruitment trajectories are calculated from CCPs over the full range of lifetimes, especially after alignment to a single event (Taylor et al., 2011). As our measurements of enDyn2-EGFP recruitment show, recruitment patterns may only become apparent when calculated for defined lifetime cohorts; bulk averages are biased toward the peak recruitment and may obscure lifetime-dependent association patterns.

Dynamin Recruitment during CCP Maturation

Despite evidence for a role of dynamin in the regulation of CCP maturation, most studies have focused on the burst of dynamin recruited at the end of maturation and its function in membrane fission (Ferguson and De Camilli, 2012; McMahon and Boucrot, 2011). Moreover, it has remained unclear to what extent the level of reported early association was correlated to overexpression of fluorescently labeled dynamin (Ehrlich et al., 2004; Taylor et al., 2011, 2012). Using the master/slave approach, we show that endogenous Dyn2-EGFP is consistently recruited within the first 20 s to a subpopulation of CCPs. Independent detection of the dynamin signal would have led to an erroneous conclusion (Doyon et al., 2011).

While the sensitivity of our measurements could not distinguish CCPs that recruited only small amounts of dynamin from those that recruited none, the rapid and presumably abortive turnover of dynamin-deficient CCPs nonetheless suggests that a threshold level of early dynamin recruitment is necessary for CCP maturation. Importantly, subpopulations of dynamin-positive and dynamin-deficient CCPs display not only differences in average lifetime but also a fundamentally different property of lifetime distribution. In the absence of detectable dynamin, the lifetime distribution of CCPs exhibits a quasi-exponential decay reminiscent of a first-order kinetic process where coat disassembly is triggered by a random event occurring at a specific rate (Figure S3A). In the presence of dynamin, the lifetime distribution of CCPs peaks at ~40 s, suggesting that early stages of maturation and CCP survival are actively regulated in a dynamin-dependent manner (Figures S3B and S3C).

Regulation of CCP Maturation by the α -Adaptin Appendage Domain

AP2 complexes act as a prime interaction hub in CME through their ability to bind a majority of EAPs and their function as the link between clathrin and the plasma membrane (Schmid and McMahon, 2007). The finding, reproduced here, that the α -adaptin appendage domain (α AD), which recruits EAPs, was dispensable for efficient CME as measured by Tfn uptake (Motley et al., 2006) was therefore unexpected and has puzzled many researchers in the field. Because many EAPs have the ability to bind to both the α AD and β -adaptin appendage domain (β AD), as well as to other CCP constituents, it was assumed that EAP recruitment and CCP maturation were maintained by these redundant interactions. However, our quantitative analysis of CCP dynamics, coupled with EM, has revealed striking phenotypes associated with loss of the α AD.

Contrary to the assumption that clathrin assembly alone drives curvature generation (Dannhauser and Ungewickell, 2012), a significant fraction of nascent CCPs in cells expressing Δ AD α -adaptin fail to gain curvature and form flat, lattice-shaped structures. These aberrant structures are distinct from recently described clathrin plaques in that they are short lived and small (≤ 200 nm). These data suggest that α AD-EAP interactions may directly or indirectly regulate clathrin assembly into curved lattices. Importantly, curved CCPs that do form in Δ AD cells undergo a more rapid and possibly less complex maturation process than those that form in control cells. Hence, α AD-EAP interactions have a fundamental effect on switching CCP maturation from an unregulated process characterized by first-order,

quasi-exponential decay kinetics into a regulated, multistep process (Figure S3). AP2-interacting EAPs could regulate clathrin assembly (e.g., auxilin), generate and/or stabilize curvature (e.g., FCHo1/2, amphiphysin, endophilin, SNX9, epsin), trigger conformational changes in AP2 to enhance cargo binding (e.g., AAK1), interact with cargo molecules (e.g., SNX9, epsin, eps15), and/or act as scaffolds (intersectin, eps15). Any of these functions could contribute to the observed requirement for α AD during the early and/or late stages of CME. Determining the identity and hierarchy of EAPs that are essential to these functions will require further studies. Given the robustness of bulk CME to the loss of EAP interactions, the assays described here will be essential for elucidating the specific functions of EAPs.

Plasticity of CME

We have identified two compensatory mechanisms that together are likely to contribute to the unexpected robustness of CME in Δ AD cells. First, the initiation rate for bona fide CCPs was approximately two times higher, potentially compensating for the higher failure rate of abortive structures in these cells. This suggests the existence of some feedback mechanism linking CCP stabilization to initiation rates and/or that α AD somehow negatively regulates the efficiency of CCP nucleation events. Second, although nonproductive, flat lattices constitute a significant proportion of CCPs in Δ AD cells, our EM and Epi:TIR ratio-based analyses reveal a significant fraction of CCPs that appear to assemble normally. CCPs that gain curvature in Δ AD cells appear to undergo maturation much more quickly and synchronously than in control cells, which could also compensate for the loss of α AD-EAP interactions. Importantly, the identification of these compensatory mechanisms and the plasticity of CME have profound implications for future studies of the mechanisms governing CME. One example of the consequence of this plasticity derives from the recently published results of a whole genome siRNA screen based on CME of Tfn: none of the 92 hits identified in this screen corresponded to known EAPs (Kozik et al., 2013). The assays we have developed will be essential for identifying the function of individual EAPs.

CCP Maturation Is Controlled by Regulatory Checkpoints that Depend on Dynamin-2 and Full-Length AP2

The shape of the CCP lifetime distributions revealed by our measurements (Figure 3C) suggests that CCP internalization can be triggered only after completion of one or more rate-limiting, regulatory steps during CCP maturation (Figure S3). The peak of the distribution indicates that key regulating steps likely occur prior to the first ~30–40 s of maturation. Indeed, the distinct lifetime distributions measured for dynamin-positive and dynamin-deficient CCPs support this hypothesis. Dynamin-positive CCPs displayed the characteristics of a multistep process with a majority of lifetimes >40 s. In contrast, the lifetime distribution of dynamin-deficient CCPs decayed quasi-exponentially, consistent with an abortive process undergoing unregulated disassembly with first-order kinetics. Analogous to this observation, the distributions of flat lattices in Δ AD cells are shifted toward shorter lifetimes and display a similar quasi-exponential decay. In contrast, the lifetime distributions of curved pits in Δ AD cells peak at ~20 s, suggesting a more rapid, and potentially less regulated process.

These data are consistent with a checkpoint model that we and others have previously proposed for CME (Henry et al., 2012; Loerke et al., 2009; Puthenveedu and von Zastrow, 2006). Prior evidence for this model includes a statistical decomposition of CCP lifetimes that showed a differential response of abortive versus productive CCP subpopulations to perturbation of dynamin function and cargo concentration (Loerke et al., 2009) and the identification of cargo-specific subpopulations of CCPs with distinct maturation kinetics (Henry et al., 2012; Liu et al., 2010; Puthenveedu and von Zastrow, 2006). There is also evidence that different EAPs (Mettlen et al., 2009b), as well as lipid kinases and phosphatases (Antonescu et al., 2011), may hierarchically act as inputs to the checkpoint. The assays we describe here provide the tools to further test this hypothesis and identify the role of individual EAPs in the regulation of CME.

EXPERIMENTAL PROCEDURES

Cell Biology

The procedures used for culture of human RPE cells, siRNA transfection, CHC immunoprecipitation, and immunoblotting are described in the [Supplemental Experimental Procedures](#) available online. Tfn receptor internalization assays were performed as previously described elsewhere (Yarar et al., 2005) and are summarized in the [Supplemental Experimental Procedures](#).

Image Acquisition

TIRF microscopy was performed as previously described elsewhere (Liu et al., 2010). Detailed acquisition parameters are provided in the [Supplemental Experimental Procedures](#).

Image and Data Analysis

The methods for model-based detection of CCSs, validation of CCS trajectories, cell-to-cell intensity normalization, identification of bona fide CCPs, master/slave-based identification of significant EAP signals, calculation of lifetime distributions, and curvature measurement by Epi:TIR ratio are detailed in the [Supplemental Experimental Procedures](#). CCS tracking was performed using the u-track software package (Jaqaman et al., 2008), and all trajectories representing fully observable (i.e., not truncated by the acquisition), diffraction-limited CCSs were retained for further analysis. All analyses were implemented in Matlab (MathWorks, Natick, MA, USA). The software is available for download as [Supplemental Software](#) and at <http://lccb.hms.harvard.edu/software.html>.

SUPPLEMENTAL INFORMATION

Supplemental Information includes Supplemental Experimental Procedures, four figures, four movies, and Supplemental Software and can be found with this article online at <http://dx.doi.org/10.1016/j.devcel.2013.06.019>.

ACKNOWLEDGMENTS

This research was supported by National Institutes of Health grants R01 GM73165 (to G.D. and S.L.S.) and MH61345 (to S.L.S.) and fellowships from the Swiss National Science Foundation (to F.A.) and the American Heart Association (to M.M.). We thank M. Wood, Director of The Scripps Research Institute Electron Microscopy Core, for EM sample preparation and imaging, and M. Leonard and V. Lukiyanchuk for technical assistance. SK-MEL-2 (Human Skin Melanoma) cells expressing CLCa-RFP and/or Dyn2-EGFP under their endogenous promoters were kindly provided by D. Drubin (University of California, Berkeley). We thank T. Kirchhausen (Harvard Medical School) for providing the dtTomato-CLCa construct and BSC1 cells stably expressing EGFP-CLCa, and we thank A. Sorkin (University of Pittsburgh Medical School) and M. Robinson (Cambridge Institute for Medical Research) for kindly providing μ 2-EGFP and siRNA-resistant α -adaplin constructs.

Received: March 29, 2013

Revised: May 15, 2013

Accepted: June 19, 2013

Published: July 25, 2013

REFERENCES

- Antonescu, C.N., Aguet, F., Danuser, G., and Schmid, S.L. (2011). Phosphatidylinositol-(4,5)-bisphosphate regulates clathrin-coated pit initiation, stabilization, and size. *Mol. Biol. Cell* 22, 2588–2600.
- Cheezum, M.K., Walker, W.F., and Guilford, W.H. (2001). Quantitative comparison of algorithms for tracking single fluorescent particles. *Biophys. J.* 81, 2378–2388.
- Cocucci, E., Aguet, F., Boulant, S., and Kirchhausen, T. (2012). The first five seconds in the life of a clathrin-coated pit. *Cell* 150, 495–507.
- Conner, S.D., and Schmid, S.L. (2003). Regulated portals of entry into the cell. *Nature* 422, 37–44.
- Damke, H., Binns, D.D., Ueda, H., Schmid, S.L., and Baba, T. (2001). Dynamin GTPase domain mutants block endocytic vesicle formation at morphologically distinct stages. *Mol. Biol. Cell* 12, 2578–2589.
- Dannhauser, P.N., and Ungewickell, E.J. (2012). Reconstitution of clathrin-coated bud and vesicle formation with minimal components. *Nat. Cell Biol.* 14, 634–639.
- Doyon, J.B., Zeitler, B., Cheng, J., Cheng, A.T., Cherone, J.M., Santiago, Y., Lee, A.H., Vo, T.D., Doyon, Y., Miller, J.C., et al. (2011). Rapid and efficient clathrin-mediated endocytosis revealed in genome-edited mammalian cells. *Nat. Cell Biol.* 13, 331–337.
- Ehrlich, M., Boll, W., Van Oijen, A., Hariharan, R., Chandran, K., Nibert, M.L., and Kirchhausen, T. (2004). Endocytosis by random initiation and stabilization of clathrin-coated pits. *Cell* 118, 591–605.
- Ferguson, S.M., and De Camilli, P. (2012). Dynamin, a membrane-remodelling GTPase. *Nat. Rev. Mol. Cell Biol.* 13, 75–88.
- Gaidarov, I., Santini, F., Warren, R.A., and Keen, J.H. (1999). Spatial control of coated-pit dynamics in living cells. *Nat. Cell Biol.* 1, 1–7.
- Girard, M., Allaire, P.D., McPherson, P.S., and Blondeau, F. (2005). Non-stoichiometric relationship between clathrin heavy and light chains revealed by quantitative comparative proteomics of clathrin-coated vesicles from brain and liver. *Mol. Cell. Proteomics* 4, 1145–1154.
- Henry, A.G., Hislop, J.N., Grove, J., Thorn, K., Marsh, M., and von Zastrow, M. (2012). Regulation of endocytic clathrin dynamics by cargo ubiquitination. *Dev. Cell* 23, 519–532.
- Huang, F., Jiang, X., and Sorkin, A. (2003). Tyrosine phosphorylation of the beta2 subunit of clathrin adaptor complex AP-2 reveals the role of a di-leucine motif in the epidermal growth factor receptor trafficking. *J. Biol. Chem.* 278, 43411–43417.
- Huang, F., Khvorova, A., Marshall, W., and Sorkin, A. (2004). Analysis of clathrin-mediated endocytosis of epidermal growth factor receptor by RNA interference. *J. Biol. Chem.* 279, 16657–16661.
- Jaqaman, K., Loerke, D., Mettlen, M., Kuwata, H., Grinstein, S., Schmid, S.L., and Danuser, G. (2008). Robust single-particle tracking in live-cell time-lapse sequences. *Nat. Methods* 5, 695–702.
- Kozik, P., Hodson, N.A., Sahlender, D.A., Simecek, N., Soromani, C., Wu, J., Collinson, L.M., and Robinson, M.S. (2013). A human genome-wide screen for regulators of clathrin-coated vesicle formation reveals an unexpected role for the V-ATPase. *Nat. Cell Biol.* 15, 50–60.
- Liu, A.P., Aguet, F., Danuser, G., and Schmid, S.L. (2010). Local clustering of transferrin receptors promotes clathrin-coated pit initiation. *J. Cell Biol.* 191, 1381–1393.
- Loerke, D., Mettlen, M., Yarar, D., Jaqaman, K., Jaqaman, H., Danuser, G., and Schmid, S.L. (2009). Cargo and dynamin regulate clathrin-coated pit maturation. *PLoS Biol.* 7, e57.
- Mattheyses, A.L., Atkinson, C.E., and Simon, S.M. (2011). Imaging single endocytic events reveals diversity in clathrin, dynamin and vesicle dynamics. *Traffic* 12, 1394–1406.

- McMahon, H.T., and Boucrot, E. (2011). Molecular mechanism and physiological functions of clathrin-mediated endocytosis. *Nat. Rev. Mol. Cell Biol.* **12**, 517–533.
- Merrifield, C.J., Feldman, M.E., Wan, L., and Almers, W. (2002). Imaging actin and dynamin recruitment during invagination of single clathrin-coated pits. *Nat. Cell Biol.* **4**, 691–698.
- Mettlen, M., Pucadyil, T., Ramachandran, R., and Schmid, S.L. (2009a). Dissecting dynamin's role in clathrin-mediated endocytosis. *Biochem. Soc. Trans.* **37**, 1022–1026.
- Mettlen, M., Stoeber, M., Loerke, D., Antonescu, C.N., Danuser, G., and Schmid, S.L. (2009b). Endocytic accessory proteins are functionally distinguished by their differential effects on the maturation of clathrin-coated pits. *Mol. Biol. Cell* **20**, 3251–3260.
- Mishra, S.K., Hawryluk, M.J., Brett, T.J., Keyel, P.A., Dupin, A.L., Jha, A., Heuser, J.E., Fremont, D.H., and Traub, L.M. (2004). Dual engagement regulation of protein interactions with the AP-2 adaptor α appendage. *J. Biol. Chem.* **279**, 46191–46203.
- Motley, A.M., Berg, N., Taylor, M.J., Sahlender, D.A., Hirst, J., Owen, D.J., and Robinson, M.S. (2006). Functional analysis of AP-2 α and μ 2 subunits. *Mol. Biol. Cell* **17**, 5298–5308.
- Praefcke, G.J.K., Ford, M.G.J., Schmid, E.M., Olesen, L.E., Gallop, J.L., Peak-Chew, S.Y., Vallis, Y., Babu, M.M., Mills, I.G., and McMahon, H.T. (2004). Evolving nature of the AP2 α -appendage hub during clathrin-coated vesicle endocytosis. *EMBO J.* **23**, 4371–4383.
- Puthenveedu, M.A., and von Zastrow, M. (2006). Cargo regulates clathrin-coated pit dynamics. *Cell* **127**, 113–124.
- Rappoport, J.Z., Taha, B.W., Lemeer, S., Benmerah, A., and Simon, S.M. (2003). The AP-2 complex is excluded from the dynamic population of plasma membrane-associated clathrin. *J. Biol. Chem.* **278**, 47357–47360.
- Saffarian, S., Cocucci, E., and Kirchhausen, T. (2009). Distinct dynamics of endocytic clathrin-coated pits and coated plaques. *PLoS Biol.* **7**, e1000191.
- Schmid, E.M., and McMahon, H.T. (2007). Integrating molecular and network biology to decode endocytosis. *Nature* **448**, 883–888.
- Schmid, S.L., and Frolov, V.A. (2011). Dynamin: functional design of a membrane fission catalyst. *Annu. Rev. Cell Dev. Biol.* **27**, 79–105.
- Sever, S., Damke, H., and Schmid, S.L. (2000). Dynamin:GTP controls the formation of constricted coated pits, the rate limiting step in clathrin-mediated endocytosis. *J. Cell Biol.* **150**, 1137–1148.
- Soulet, F., Yarar, D., Leonard, M., and Schmid, S.L. (2005). SNX9 regulates dynamin assembly and is required for efficient clathrin-mediated endocytosis. *Mol. Biol. Cell* **16**, 2058–2067.
- Taylor, M.J., Perrais, D., and Merrifield, C.J. (2011). A high precision survey of the molecular dynamics of mammalian clathrin-mediated endocytosis. *PLoS Biol.* **9**, e1000604.
- Taylor, M.J., Lampe, M., and Merrifield, C.J. (2012). A feedback loop between dynamin and actin recruitment during clathrin-mediated endocytosis. *PLoS Biol.* **10**, e1001302.
- Traub, L.M. (2009). Tickets to ride: selecting cargo for clathrin-regulated internalization. *Nat. Rev. Mol. Cell Biol.* **10**, 583–596.
- Yarar, D., Waterman-Storer, C.M., and Schmid, S.L. (2005). A dynamic actin cytoskeleton functions at multiple stages of clathrin-mediated endocytosis. *Mol. Biol. Cell* **16**, 964–975.

Developmental Cell, Volume 26

Supplemental Information

Advances in Analysis of Low Signal-to-Noise Images Link Dynamin and AP2 to the Functions of an Endocytic Checkpoint

**François Aguet, Costin N. Antonescu, Marcel Mettlen, Sandra L. Schmid, and
Gaudenz Danuser**

Inventory of supplemental materials:

- **Supplemental Figures S1–S4**
Figure S1, related to Figure 1
Figure S2, related to Figure 1
Figure S3, related to Figure 3
Figure S4, related to Figure 5
- **Supplemental Movies S1–S4**
Movie S1, related to Figure 1
Movie S2, related to Figure 1
Movie S3, related to Figure 4
Movie S4, related to Figure 5
- **Supplemental Experimental Procedures**
- **Supplemental References**
- **Supplemental Software**

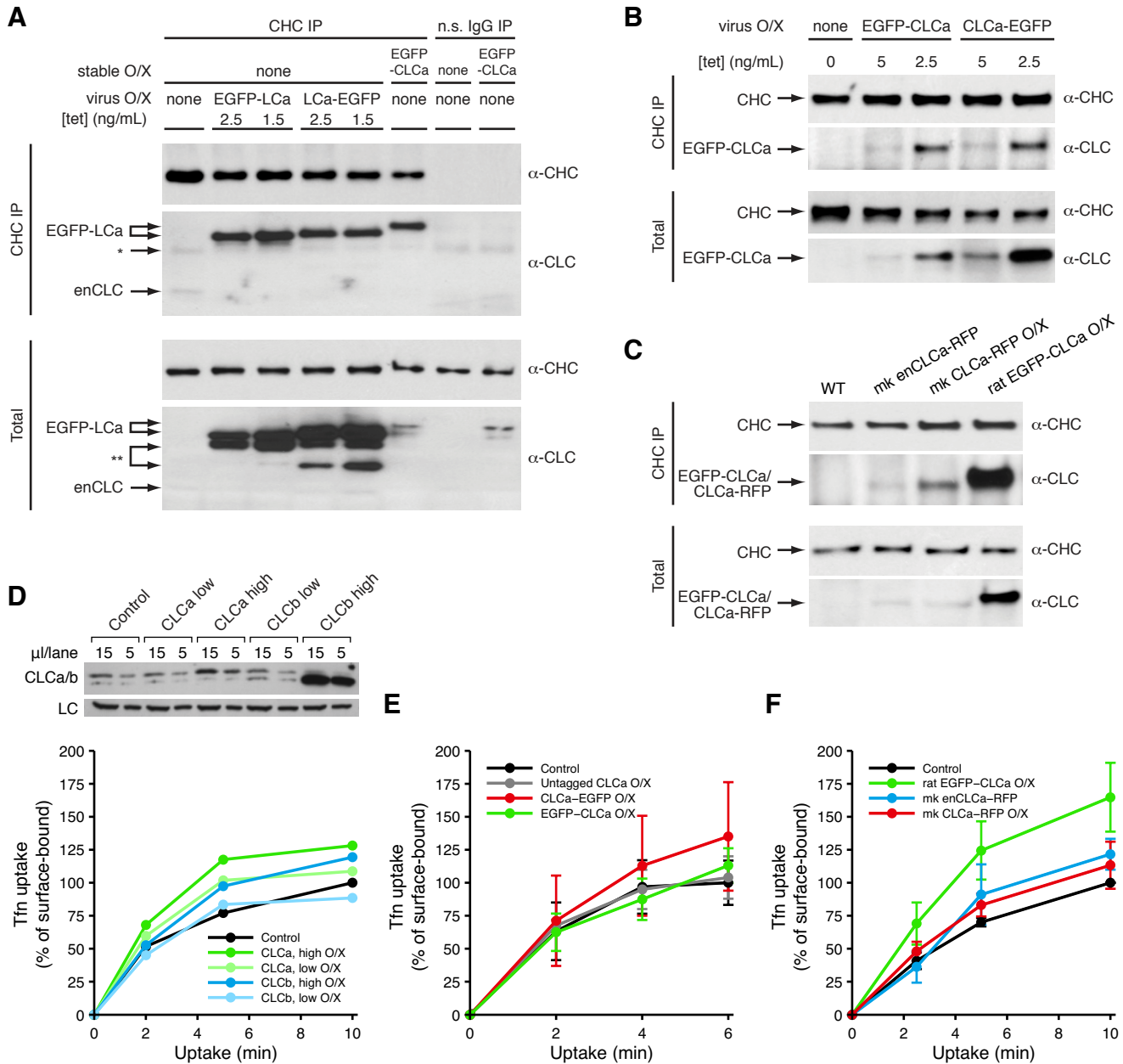


Figure S1. Over-expressed clathrin light chains are incorporated into clathrin triskelions and do not affect CME, related to Figure 1 (A) Clathrin heavy chain (CHC) was immunoprecipitated from cells overexpressing either N- or C-terminally EGFP-tagged rat CLCa from tet-regulatable adenoviral vectors. The fluorescently-tagged light chains are incorporated into clathrin triskelions at a much higher stoichiometry than endogenous CLCa in uninfected control cells or in genome-edited enEGFP-CLCa cells. Unincorporated CLCa is partially degraded as can be seen in western blots of the whole cell lysate (total). * indicates a non-specific band and ** indicates degradation products. (B) N-terminally tagged CLCa is more efficiently incorporated into triskelions than C-terminally-tagged CLCa, although both are co-precipitated with CHC. (C) CLCa from monkey and rat are equally efficiently incorporated into CHC in monkey BSC1 cells. (D) Transferrin uptake is unaffected in HeLa cells over-expressing CLCa or CLCb at either low or high levels, as determined by western blots (top). LC: loading control. (E) Transferrin uptake in HeLa cells over-expressing untagged CLCa, or CLCa fused to EGFP at the N- or C-terminus (error bars: s.d. from 3 experiments). (F) Transferrin uptake in stably transformed BSC1 cells over-expressing either rat or monkey CLCa or genome-edited to express monkey CLCa-RFP from its endogenous locus, as indicated (error bars: s.d. from 3 experiments).

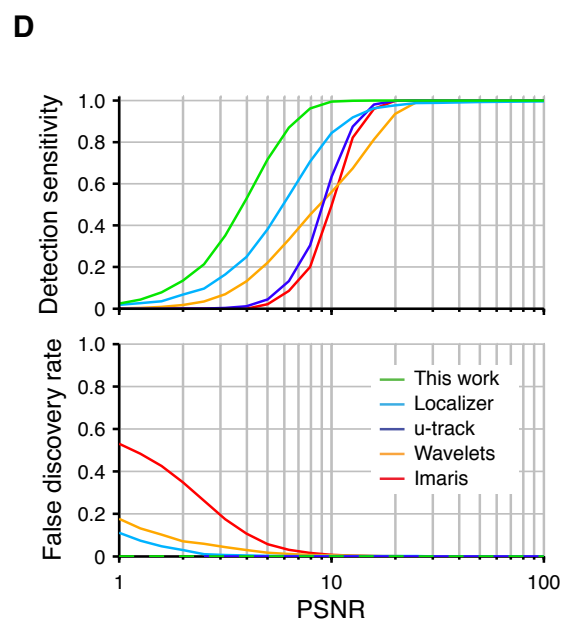
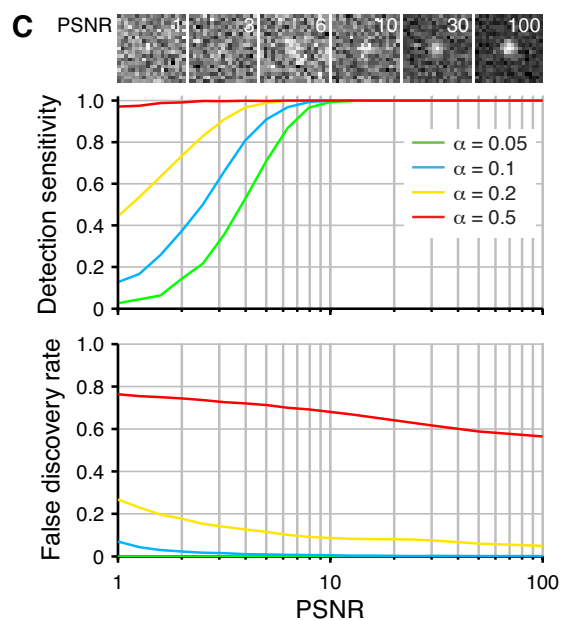
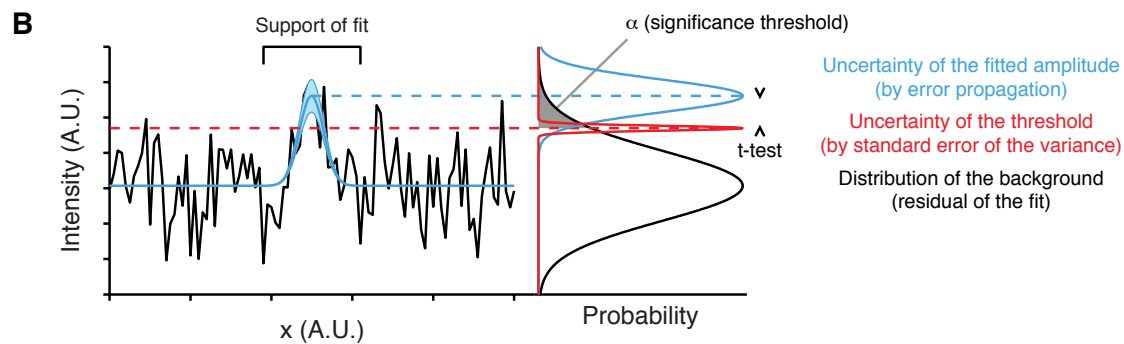
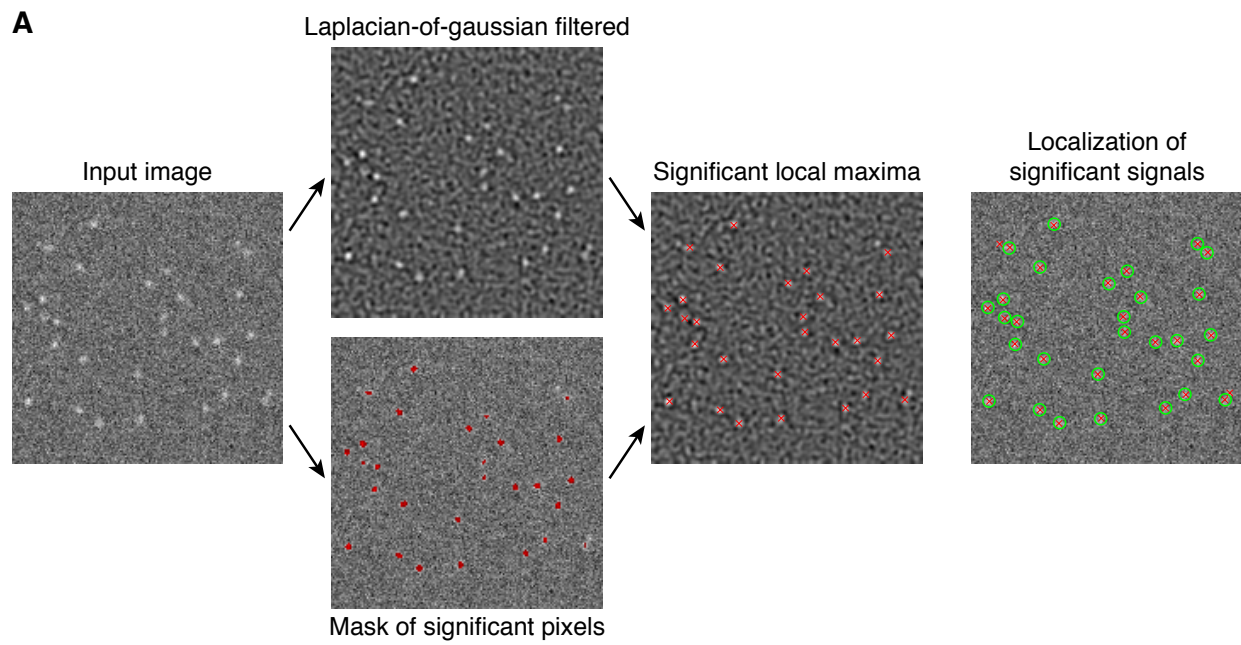


Figure S2. Model-based detection of diffraction-limited fluorescence signals, related to Figure 1 (A) Flow of spot detection algorithm on simulated noisy data. Input image is filtered with two separate filters, one based on the detection model to identify pixels with significant signal (see Supplemental Experimental Procedures), and a Laplacian-of-Gaussian

to identify local maxima. Local maxima at significant locations are used to initialize model fitting, which determines estimates of fluorescence signal amplitude, local background, and sub-pixel location (see Supplemental Experimental Procedures). **(B)** Selection of significant spot signals, illustrated for a 1-D cross-section of a diffraction-limited signal. A Gaussian function approximating the point-spread function (PSF) of the microscope (blue) is fitted to the raw intensities (black), with amplitude, local background, and position as free parameters. The spread of the Gaussian approximation is defined by the PSF. Residuals of the fit yield the noise distribution and, by error propagation, the uncertainty on the fitted amplitude (blue shaded area). The amplitude is considered significant if it lies above a threshold value in the noise distribution, shown here for the 95th percentile. The uncertainty on this threshold is calculated from the standard error of the variance (red). Significance is determined with a one-tailed, two-sample t-test. For details, see Supplemental Experimental Procedures. **(C)** Performance of the detection as a function of the significance threshold α defined in Panel B, calculated on simulated noisy data containing Gaussian-shaped signals of varying amplitude with additive white Gaussian noise, corresponding to a PSNR ranging from 1 to 100 (PSNR was defined as $\max(\text{signal})^2/\text{MSE}$ and MSE is the mean squared error between the true and noisy signal). Detection sensitivity is the proportion of correctly identified signals, and the false discovery rate is the ratio of false positive detections to total detections. **(D)** Comparison of detection performance between the proposed algorithm and several state-of-the-art methods. Performance was assessed on simulated noisy data containing Gaussian-shaped signals of varying amplitude with additive white Gaussian noise, corresponding to a PSNR ranging from 1 to 100. All algorithms were tested using their default, automatic settings unless otherwise noted. The standard deviation of the Gaussian spots was set to 1.4 pixels. Wavelets denotes an approach using wavelet multi-scale products previously used for CCP and endosome detection (Loerke et al. 2009, Olivo-Marin 2002); Imaris denotes the DetectSpots2 function included in the Imaris 7.5 software package, where a spot diameter of 5 pixels was selected. This method was used by (Doyon et al., 2011) for CCP detection based on endogenously labeled CLCa and dynamin; u-track denotes the u-track software package (Jaqaman et al., 2008); Localizer denotes the Localizer software package designed for STORM/PALM applications. The method relies on a generalized likelihood ratio test to assess significance (Dedecker et al., 2012), with 'glrt' parameter set to 15 (at the default value of 25, its performance is slightly inferior to u-track).

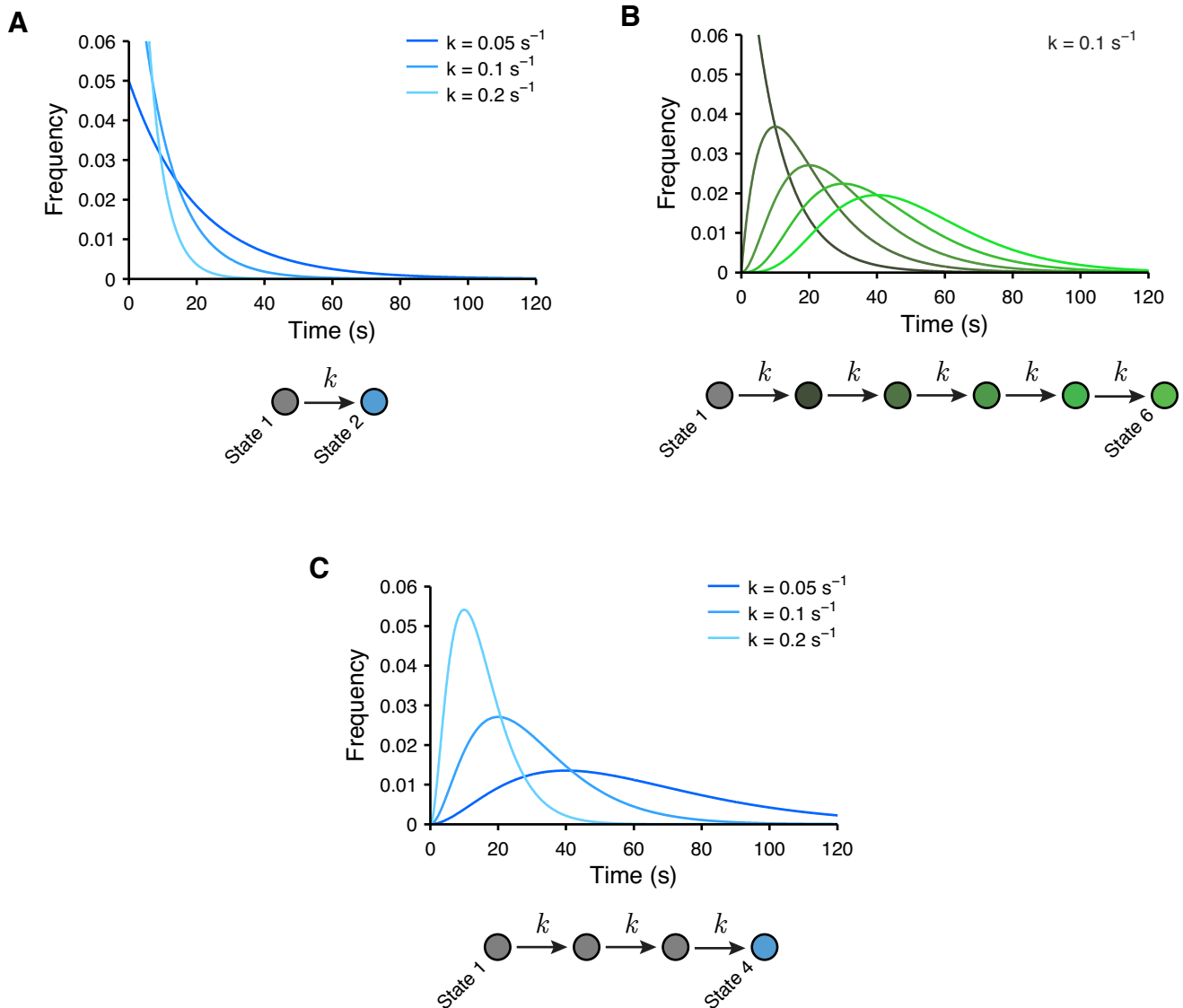


Figure S3. Lifetime distributions generated by single-step and regulated multi-step processes, related to Figure 3 (A) An unregulated process driven by a single rate constant k generates exponentially distributed lifetimes. (B) A process regulated by transitions through multiple states yields lifetime distributions that display a characteristic rise and decay. The distributions become more spread and are shifted towards longer lifetimes as the number of steps increases. Processes with variable rates among the different steps generate distributions with shapes comparable to those shown. (C) For a fixed number of steps, changes in the rate constant(s) produces a scaling effect. Limited to the models described here, the lifetime distribution of CCPs that recruited dynamin (Figure 5, Panel E) is best reproduced by a three-stage process. This is consistent with the statistical decomposition of lifetime distributions in (Loerke et al., 2009), which revealed three populations of CCPs.

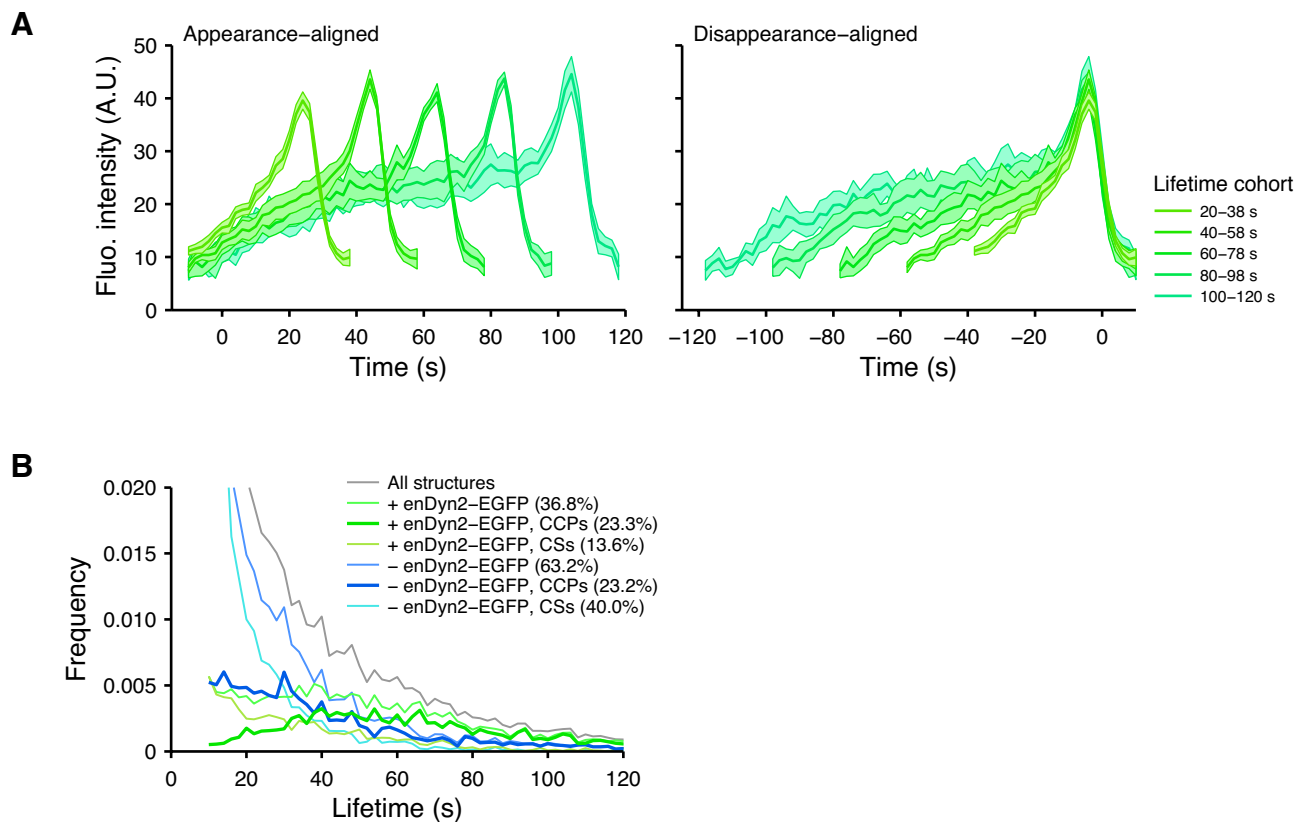


Figure S4. Measurement of dynamin recruitment, related to Figure 5 (A) Average traces of dynamin fluorescence intensity in SK-MEL-2 cells with endogenously-tagged enDyn2-EGFP and overexpressing tdTomato-CLCa. Trajectories were selected for CCPs that recruited detectable enDyn2-EGFP. Averages were calculated for each indicated lifetime cohort from trajectories interpolated to the mean cohort lifetime, and were subsequently aligned by their first (left) or last time point (right). **(B)** Lifetime distributions of all CCSs classified as a function of enDyn2-EGFP recruitment and the intensity threshold described in Figures 2 & 3.

Supplemental Movies

Movie S1. Model-based detection of clathrin-coated structures in EGFP-CLCa over-expressing cells imaged by TIRFM, related to Figure 1. The movie corresponds to the EGFP-CLCa O/X frames shown in Figure 1, Panel A. Red patches indicate pixels detected as significant by a wavelet-based method and green circles indicate the positions of CCSs detected with the model-based algorithm proposed in this work (see Supplemental Experimental Procedures). False-positives (orange circles) and false-negatives (white circles) of the wavelet-based method are in reference to the model-based detections. Scale bar: 2 μm .

Movie S2. Model-based detection of clathrin-coated structures in genome-edited enCLCa-RFP cells imaged by TIRFM, related to Figure 1. The movie corresponds to the enCLCa-RFP frames shown in Figure 1, Panel A. Red patches indicate pixels detected as significant by a wavelet-based method and green circles indicate the positions of CCSs detected with the model-based algorithm proposed in this work (see Supplemental Experimental Procedures). False-positives (orange circles) and false-negatives (white circles) of the wavelet-based method are in reference to the model-based detections. Scale bar: 2 μm .

Movie S3. Master/slave detection of CCSs by $\mu\text{2-EGFP}$ in genome-edited enCLC-RFP cells, related to Figure 4. CCSs were detected in the $\mu\text{2-EGFP}$ “master” channel (green circles); fluorescence intensities in the enCLCa-RFP “slave” channel were measured by sub-pixel localization at the detected $\mu\text{2-EGFP}$ positions (red circles). The small shifts between the positions in the master and slave channels (overlay) are due to the effect of noise on the individual localizations and the motion of CCSs between acquisitions of the two channels. Scale bar: 2 μm .

Movie S4. Master/slave detection of early dynamin recruitment in genome-edited enDyn2-EGFP cells overexpressing tdTomato-CLCa, related to Figure 5. CCSs were detected in the tdTomato-CLCa “master” channel (red circles); fluorescence intensities in the enDyn2-EGFP “slave” channel were measured by sub-pixel localization at the detected tdTomato-CLCa positions. Color code: green, independently detectable enDyn2-EGFP; blue, significant enDyn2-EGFP fluorescence relative to enDyn2-EGFP fluorescence outside of CCSs; gray, undetectable enDyn2-EGFP. The small shifts between the positions in the master and slave channels (overlay) are due to the effect of noise on the individual localizations and the motion of CCSs between acquisitions of the two channels. Scale bar: 2 μm .

SUPPLEMENTAL EXPERIMENTAL PROCEDURES

Cells and cell culture

RPE (retinal pigment epithelial) cells stably expressing EGFP-CLCa were generated through infection with retroviruses (described in (Liu et al., 2008)) coding for EGFP-CLCa in a pMIEG3 vector, followed by FACS sorting. SK-MEL-2 (Human Skin Melanoma) cells, expressing CLCa-RFP and/or Dyn2-EGFP under the endogenous promoter were kindly provided by D. Drubin (University of California, Berkeley). As indicated, these cells were transiently transfected with dtTomato-CLCa (kindly provided by T. Kirchhausen, Harvard Medical School) or the $\mu 2$ subunit of AP2, tagged with EGFP that was inserted between residues 236 and 237 of an internal disordered loop (kindly provided by S. Sorkin, University of Pittsburgh Medical School), using Lipofectamine 2000 (Life Technologies, Carlsbad, CA) according to the manufacturer's instructions. RPE cells stably expressing full-length (FL) or ΔAD α -adaptin were generated as follows: cDNA encoding the FL or truncated ΔAD α -adaptin, kindly provided by M.S. Robinson (Motley et al., 2006), were subcloned into the pMIEG3 retroviral vector. cDNA encoding mTagBFP (Subach et al., 2008) was subcloned into an IRES downstream of the α -adaptin sequence within the pMIEG3 vector. Each α -adaptin pMIEG3-mTagBFP construct was used to generate retroviruses. RPE cells stably expressing EGFP-CLCa were infected with each resulting retrovirus, followed by FACS to sort cells into nearly homogenous BFP expression cohorts. Note that BFP expression is proportional to the expression of each α -adaptin protein. Expression of α -adaptins within each stable cell cohort was determined by Western blotting with α -adaptin antibodies; the cohort with the expression level closest to endogenous α -adaptin was chosen for further experiments. Cells infected with similar retroviruses expressing only BFP served as the BFP control. All cells were grown under 5% CO₂ at 37°C in DMEM/Ham's F12 medium supplemented with 20 mM HEPES, 10 mg/ml streptomycin, 66 μ g/ml penicillin and 10% (v/v) and fetal calf serum (FCS, HyClone).

siRNA transfection

RPE cells were treated with a previously established siRNA sequence (Motley et al., 2006) using RNAiMAX (Life Technologies, Carlsbad, CA) to silence endogenous α -adaptin following the manufacturer's instructions. Briefly, 110 pmol of α -adaptin siRNA and 6.25 μ l of RNAiMAX reagent were added in 2 ml of OptiMEM in each well of a 6-well plate of RPE cells for 4 hours. Transfection was performed twice, 72h and 48h prior to experiments. Note that exogenous FL or ΔAD α -adaptin (Motley et al., 2006) harbor mutations that confer resistance to siRNA silencing.

Transferrin receptor internalization

Transferrin (Tfn) internalization was performed as previously described (Yarar et al., 2005), using either biotinylated Tfn (BSST) or biotinylated anti-TfnR mAb, B-D65, as ligand. Briefly, RPE cells grown on 15-cm dishes were detached with PBS supplemented with 5 mM EDTA and resuspended in Tfn assay buffer (PBS supplemented with 1 mM MgCl₂, 1 mM CaCl₂, 5 mM glucose, and 0.2% bovine serum albumin). Suspended cells were incubated with either 5 μ g/ml BSST or B-D65 at 37°C for indicated times followed by immediate cooling to 4°C to arrest internalization. Following washing to remove unbound ligand, surface bound ligand was quenched by sequential incubation with free avidin (0.05 mg/ml) and biocytin (0.05 mg/ml). Cell lysates were prepared by solubilization in blocking buffer (1% TX-100, 0.1% SDS, 0.2% BSA, 50 mM NaCl, and 1 mM Tris, pH 7.4) and plated onto ELISA plates coated with anti-transferrin (Scottish Antibody Production Unit, Carlisle, Scotland) or anti-mslgG (Sigma-Aldrich) and assayed for protected/internalized B-ligand using streptavidin-POD (Roche). Internalized ligand is expressed as the percent of the total surface bound at 4°C (i.e., not quenched with avidin), measured in parallel.

Clathrin heavy chain immunoprecipitation

RPE cell lines either stably expressing CLCa/b fusion proteins or infected with adenoviruses encoding EGFP-CLCa/b or CLCa/b-EGFP were lysed in 250-400 μ l buffer containing 50 mM HEPES, pH 7.4, 300 mM NaCl, 5 mM EDTA and 1% TX-100 and protease inhibitor cocktail (Sigma-Aldrich). Cell lysates were passed through a 27.5 gauge syringe 5 times and cell debris was removed by centrifugation at 12k rpm for 15 min. X22 anti-clathrin antibodies were pre-bound to Protein G Sepharose 4 (GE Healthcare) and then incubated with the cell lysates for 4h under constant rotation. Subsequently, unbound proteins were removed and beads were washed 5 times by sequential centrifugation and resuspension in wash buffer (50 mM HEPES, pH 7.4, 300 mM NaCl, 5 mM EDTA and 0.1% TX-100). Immuno-precipitated proteins were

resolved by SDS-PAGE followed by immunoblotting with either anti-clathrin heavy chain (TD.1) or an anti-CLC rabbit polyclonal generated in the Schmid lab.

Immunoblotting

Whole cell lysates were prepared from cells grown on six-well plates as previously described (Antonescu et al., 2010). Briefly, cells were lysed by adding 300 μ l of 2 \times Laemmli sample buffer (2 \times LSB: 0.125 M Tris, pH 6.8, 2% SDS (wt/vol), 5% glycerol (vol/vol), and 7.5% β -mercaptoethanol (vol/vol), supplemented with protease inhibitor cocktail (Sigma-Aldrich). Equal amounts of total protein of each sample were resolved by SDS-PAGE followed by immunoblotting using the following antibodies: anti-endogenous α -adaptin (100/2, Sigma-Aldrich), anti-exogenous α -adaptin (Motley et al., 2006), anti- β 1/2 adaptin (100/1, Sigma-Aldrich), μ 2-adaptin (AP-50, BD Transduction Labs). Anti-HSP40 (Enzo Life Sciences) was used as a loading control.

TIRF microscopy

Total internal reflection fluorescence (TIRF) microscopy was performed as previously described (Loerke et al., 2009). Briefly, RPE cells expressing EGFP-CLCa were imaged using a 100 \times 1.49 NA Apo TIRF objective (Nikon) mounted on a Ti-Eclipse inverted microscope with equipped with the Perfect Focus System (Nikon). During imaging, cells were maintained in DMEM lacking phenol red and supplemented with 2.5% fetal calf serum. Time-lapse image sequences from different cells were acquired at a frame rate of 1 frame \cdot s⁻¹ and exposure time of 100-120ms using a CoolSNAP HQ2 monochrome CCD camera with 6.45 \times 6.45 μ m² pixels (Photometrics, Tuscon, AZ). Similarly, nearly simultaneous 2-channel (e.g. 488 nm epifluorescence/TIRF or 488nm/561nm TIRF) movies were acquired at 0.5 frame \cdot s⁻¹ with exposure times for epifluorescence excitation of 50-100 ms (overexpressed EGFP-CLCa), and for TIRF excitation of 100-200 ms (overexpressed EGFP-CLCa or tdTomato-CLCa) or of 900 ms (CLCa-RFP and Dyn2-EGFP under the endogenous promoter).

Image and data analysis

All image and data analyses were carried out in Matlab (MathWorks, Natick, MA), using custom-written software. The software is available for download as Supplementary Software. This version constitutes a snapshot of the software at the time of publication and will not be maintained. Up-to-date versions of the software will be made available at <http://lccb.hms.harvard.edu/software.html>.

Automated detection of clathrin-coated structures

Diffraction-limited fluorescence signals are most accurately measured by fitting with a model of the microscope point spread function (PSF), which is equivalent to deconvolution of the position and intensity of the fluorescent source. This approach has been widely applied to single molecule tracking (Jaqaman et al., 2008; Sergé et al., 2008) and super-resolution microscopy based on localization of fluorescent emitters such as PALM and STORM (Patterson et al., 2010). In practice, the PSF for in-focus signals is well approximated by a 2-D Gaussian function, which renders the numerical fitting of millions of individual signals computationally tractable.

Algorithms for Gaussian-based detection and localization of fluorescent point sources generally comprise three sequential operations: 1) identification of locations with sufficient probability of containing a point-source signal; 2) estimation of the intensity and sub-pixel localization of these signals by numerical fitting with a 2-D Gaussian; 3) selection of signals considered statistically significant. Step 1) typically consists in selecting the local maxima of a denoised or smoothed version of the input image. The robustness of the criteria applied during Step 3) directly influences the sensitivity and selectivity of the approach. In super-resolution applications where SNR is generally high due to the absence of a strong background signal, a hard threshold on the amplitudes of the fitted signals relative to the estimated variance of the background noise is generally applied (Henriques et al., 2010; Holden et al., 2011; Wolter et al., 2012). As an alternative to such thresholds, which become arbitrary at lower SNRs, an approach testing for the presence of a significant signal by means of a generalized likelihood ratio test has been proposed and shown to improve detection performance (Dedecker et al., 2012).

In this work, we show that by taking into account the uncertainties of the fitted amplitude and local background when individually testing for the significance of each candidate signal, detection sensitivity and selectivity can be significantly increased over existing single-molecule detection methods. This constitutes the key innovation of the proposed detection approach.

In the derivation of this framework, we make the assumption that the fluorescent signals measured from CCSs can be described by a Gaussian PSF function and by an additive white Gaussian noise term. For the signal and noise levels observed on our experimental setup this is a valid approximation, confirmed by testing for normality with the Anderson-Darling test on areas of homogenous background and the residuals of individual fits (note that for photon counts greater than ~ 20 , the Poisson distribution is statistically indistinguishable from a Gaussian, up to a shift in mean). We also assume that the background fluorescence signal beneath each CCS can be locally approximated as constant.

To maximize computational efficiency, the proposed approach was implemented in two steps: a first pass where the amplitude and background are estimated at each pixel by fitting a Gaussian centered on the pixel; this is achieved via linear combinations of three filtering steps and yields a mask of candidate locations for fitting. In the second step, local maxima of the smoothed input image that coincide with this mask are used for initialization of a 2D-Gaussian PSF fit that yields sub-pixel localization and precise estimation of the fluorescence intensity emitted by each CCS.

The image of a CCS was modeled as

$$h[\mathbf{x}; \boldsymbol{\mu}, A, c] = Ag[\mathbf{x}; \boldsymbol{\mu}, \sigma] + c + n[\mathbf{x}]$$

where $\mathbf{x} = [x_1, x_2]$ are discrete pixel coordinates, A is the fluorescence amplitude, c is a constant representing the local background intensity for this CCS, and $g[\mathbf{x}; \boldsymbol{\mu}, \sigma] = \exp(-((x_1 - \mu_1)^2 + (x_2 - \mu_2)^2)/(2\sigma^2))$ defines the Gaussian approximation of the microscope PSF. The standard deviation σ is a fixed parameter and will be omitted from the notation for simplicity. The estimation of σ is described at the end of this section. Noise was assumed to follow a Gaussian distribution with standard deviation σ_r over the support of the CCS, i.e., $n[\mathbf{x}] \sim \mathcal{N}(0, \sigma_r^2)$. The parameters $\boldsymbol{\mu}$, A and c of the model were estimated around a candidate location $\mathbf{k} = [k_1, k_2]$ in an image frame $f[\mathbf{x}]$ by sub-pixel localization through the minimization of

$$v = \sum_{\mathbf{x} \in S} (h[\mathbf{x}; \boldsymbol{\mu}, A, c] - f[\mathbf{k} - \mathbf{x}])^2 \quad (1)$$

The spatial support for this minimization was defined as $S: \mathbf{x} \in (-[4\sigma], \dots, [4\sigma]) \times (-[4\sigma], \dots, [4\sigma])$ centered on \mathbf{k} . CCS fluorescence was considered significant and retained for further analysis if the estimated amplitude \hat{A} was above a defined threshold level of the local background noise distribution (see below).

Step 1) Pixel-level identification of statistically significant signals

Candidate positions for Gaussian-shaped signals may be obtained as the local maxima of a Laplacian-of-Gaussian-filtered (LoG) version of the input image. In noisy data containing sparse signals such as CCS fluorescence, most of the positions returned by this approach correspond to small fluctuations in the background rather than true signal positions. Performing a Gaussian fit at each position to determine signal strength is computationally inefficient and becomes intractable when applied to the $>10^7$ of positions detected in the frames of a typical time-series. This can be circumvented by first calculating estimates of A and c at the pixel locations of f to generate a pixel-level mask of significant signal positions. Sub-pixel localization can then be performed for the LoG local maxima that fall within this mask (see Figure S2). A pixel-level mask of significant signal positions is obtained by minimizing

$$v = \sum_{\mathbf{x} \in S} (h[\mathbf{x}; \mathbf{0}, A, c] - f[\mathbf{k} - \mathbf{x}])^2$$

at each pixel \mathbf{k} in frame f , i.e., by minimizing

$$v[\mathbf{k}] = \sum_{\mathbf{x} \in S} (Ag[\mathbf{x}] + c - f[\mathbf{k} - \mathbf{x}])^2$$

where $g[\mathbf{x}]$ denotes $g[\mathbf{x}; \mathbf{0}]$. Specifically, estimates of the amplitude A and local background c for the Gaussian centered at each pixel \mathbf{k} are obtained by solving the system

$$\frac{\partial v[\mathbf{k}]}{\partial A} = \sum_{\mathbf{x} \in S} 2g[\mathbf{x}](Ag[\mathbf{x}] + c - f[\mathbf{k} - \mathbf{x}]) = 0$$

$$\frac{\partial v[\mathbf{k}]}{\partial c} = \sum_{\mathbf{x} \in S} 2(Ag[\mathbf{x}] + c - f[\mathbf{k} - \mathbf{x}]) = 0$$

which yields

$$\hat{A}[\mathbf{k}] = \frac{\sum_{\mathbf{x} \in S} f[\mathbf{k} - \mathbf{x}] g[\mathbf{x}] - \frac{1}{n} (\sum_{\mathbf{x} \in S} g[\mathbf{x}]) (\sum_{\mathbf{x} \in S} f[\mathbf{k} - \mathbf{x}])}{\sum_{\mathbf{x} \in S} g[\mathbf{x}]^2 - \frac{1}{n} (\sum_{\mathbf{x} \in S} g[\mathbf{x}])^2}$$

$$\hat{c}[\mathbf{k}] = \frac{\sum_{\mathbf{x} \in S} f[\mathbf{k} - \mathbf{x}] - \hat{A}[\mathbf{k}] \sum_{\mathbf{x} \in S} g[\mathbf{x}]}{n}$$

where n is the number of pixels in S . By defining $\gamma_1 = \sum_{\mathbf{x} \in S} g[\mathbf{x}]$ and $\gamma_2 = \sum_{\mathbf{x} \in S} g[\mathbf{x}]^2$ (this is numerically more accurate than using the corresponding analytical values), the above equations can be rewritten as

$$\hat{A}[\mathbf{k}] = \frac{(f * g)[\mathbf{k}] - \frac{1}{n} \gamma_1 (f * u)[\mathbf{k}]}{\gamma_2 - \frac{1}{n} \gamma_1^2}$$

$$\hat{c}[\mathbf{k}] = \frac{(f * u)[\mathbf{k}] - \gamma_1 \hat{A}[\mathbf{k}]}{n}$$

where $*$ denotes convolution and $u[\mathbf{x}]$ is a summation filter defined over S , i.e., $u[\mathbf{x}] = 1$ if $\mathbf{x} \in S$; 0 otherwise.

To identify pixels with a significant value of \hat{A} by means of a statistical test, estimates of the uncertainties on \hat{A} and the background noise, given by the residuals of the fit, are needed. At each pixel \mathbf{k} , the residual sum of squares (RSS) of the fit is given by

$$\text{RSS}[\mathbf{k}] = \gamma_2 \hat{A}[\mathbf{k}]^2 - 2 \hat{A}[\mathbf{k}] ((f * g)[\mathbf{k}] - \gamma_1 \hat{c}[\mathbf{k}]) + (f^2 * u)[\mathbf{k}] - 2 \hat{c}[\mathbf{k}] (f * u)[\mathbf{k}] + n \hat{c}[\mathbf{k}]^2$$

and the variance of the residuals is calculated as

$$\sigma_r^2[\mathbf{k}] = \frac{\text{RSS}[\mathbf{k}] - (\gamma_1 \hat{A}[\mathbf{k}] + n \hat{c}[\mathbf{k}] - (f * u)[\mathbf{k}])/n}{n - 1}$$

The uncertainty (standard deviation) on $\hat{A}[\mathbf{k}]$ is obtained by error propagation:

$$\sigma_A[\mathbf{k}] = \sqrt{\frac{\text{RSS}[\mathbf{k}]}{n - 3} [(\mathbf{J}^T)^{-1}]_{1,1}}$$

where $\mathbf{J} = [\mathbf{g} \ \mathbf{1}]$ is the Jacobian matrix (identical for all pixel positions), and \mathbf{g} is the column-vector representation of $g[\mathbf{x}]$ and $\mathbf{1}$ is the unit vector. The probability densities of the fluorescence amplitude and noise in support S at each pixel are thus $\mathcal{N}(\hat{A}[\mathbf{k}], \sigma_A^2[\mathbf{k}])$ and $\mathcal{N}(0, \sigma_r^2[\mathbf{k}])$, respectively.

An estimated amplitude was considered significant if its value was above a threshold value $\kappa \sigma_r$ of the noise distribution, where $\kappa = \sqrt{2} \text{erf}^{-1}(1 - 2\alpha)$ and α is the significance level (i.e., $\alpha = 0.05$). Significance was determined using a one-sided, two-sample t-test with $H_0: \hat{A} \leq \kappa \sigma_r$, yielding the statistic

$$T[\mathbf{k}] = \sqrt{n} \frac{\hat{A}[\mathbf{k}] - \kappa \sigma_r[\mathbf{k}]}{\sqrt{\sigma_A^2[\mathbf{k}] + \kappa^2 \sigma_r^2[\mathbf{k}]}} \quad (2)$$

where the uncertainty on σ_r was calculated using an estimator for the standard error of the variance:

$$s_r[\mathbf{k}] \approx \frac{\sigma_r[\mathbf{k}]}{\sqrt{2(n-1)}}$$

A mask of significant pixels was then defined as $m[\mathbf{k}] := p[\mathbf{k}] < \alpha$, where p is the p-value of the test.

Step 2) Sub-pixel localization and amplitude estimation

Candidate locations for 2-D Gaussian fitting were identified by selecting the local maxima of the Laplacian-of-Gaussian filtered input image that coincided with the mask $m[k]$ (see Figure S2). The standard deviation of the underlying Gaussian kernel was σ .

At each candidate location, a Gaussian fit was performed by minimization of Eq. 1, yielding estimates of A , c and μ at sub-pixel resolution. The significance of the resulting amplitude estimate \hat{A} was then tested using Eq. 2.

In areas of high CCS density, individual local maxima occurring within the same mask region were either localized individually, or through a mixture-model extension of the proposed approach replacing the single Gaussian in Eq. 1 with a sum of Gaussians. In the latter case, automated selection of the optimal number of mixture components was performed based on iterative F-tests incrementally identifying the statistical justification for additional components. In all instances, each estimated amplitude was individually tested for significance based on the criterion of Eq. 2.

The algorithm was implemented as a C/MEX function for Matlab (MathWorks, Natick, MA) using non-linear optimization routines from the GNU Scientific Library (<http://www.gnu.org/software/gsl/>). These routines provide a robust and efficient implementation of the widely used Levenberg-Marquardt algorithm.

The standard deviation σ of the 2-D Gaussian PSF was calculated either by fitting a Gaussian to a physical PSF model (Aguet et al., 2009), or by running the fitting step of the algorithm on a limited set of frames with σ as a free parameter, and selecting the most probable value. On the imaging setup used, the two approaches yielded values in agreement within <10% of each other.

Automated tracking of clathrin-coated structures

CCS trajectories were calculated from the detections obtained in individual frames using the u-track software package (Jaqaman et al., 2008). Tracking was performed using positional information only (ignoring amplitude values), and merging and splitting of tracks was enabled. CCSs forming in close vicinity (i.e., within the search radius used for linking individual detections) were thus identified as compound tracks. Examples of such tracks include dense and intersecting clusters of CCSs, or larger structures from which multiple CCPs bud off. Compound tracks can contain a combination of splitting events (branching of two trajectories from a parent trajectory) and/or merging events (fusion of two trajectories into a single trajectory).

The principal tracking parameters used were: maximum gap length: 2 or 3 frames; minimum track length: 1 frame; minimum/maximum search radius for CCSs between consecutive frames: 3/6 or 5/10 pixels. The complete set of parameters is given in the table below.

gapCloseParam	
timeWindow	3-4 or larger
mergeSplit	1
minTrackLen	1
diagnostics	0
costMatrices(1)	
funcName	costMatLinearMotionLink2
linearMotion	0
minSearchRadius	3-5
maxSearchRadius	6-10
brownStdMult	3
useLocalDensity	1
nnWindow	timeWindow
kalmanInitParam	[]
diagnostics	[]
costMatrices(2)	
funcName	costMatLinearMotionCloseGaps2
linearMotion	0
minSearchRadius	3-5
maxSearchRadius	6-10
brownStdMult	3*timeWindow
linScaling	[1 0.01]
timeReachConfL	timeWindow
maxAngleVV	[]
gapPenalty	[]
resLimit	[]

For detailed information on these parameters the reader is referred to the Supplementary Materials of (Jaqaman et al., 2008).

Gap closing accuracy

At the SNR levels obtained in EGFP-CLCa O/X cells, the gap-closing mechanism of the u-track software package is capable of identifying and filling in occasional detection misses, which typically last 1 (~60-70% of gaps) or 2 (~20% of gaps) frames. We validated closed gaps by ensuring that intensity levels always exceeded those of true background.

The maximal duration of potential gaps is constrained by the density of CCPs and the existence of hotspots (Nunez et al., 2011). In both cases, individual events occurring in close vicinity may be erroneously linked together. To avoid a high rate of false positive gaps, the duration limit for gaps was therefore set to 3 frames.

Post-processing of tracks

The trajectories returned by the u-track software were further analyzed and processed to identify signals corresponding to complete observations of assembling CCSs, as opposed to partial tracks, or compound tracks arising from ambiguities in tracking overlapping detections in areas with a high density of CCSs. This was achieved through the following steps:

1. Conversion of simple compound tracks

Compound tracks that consisted of a primary track from/to which short track segments (<5 frames) split/merged were converted into regular tracks consisting of the primary segment alone. This simplification was conditional on the last time point of each splitting segment occurring before the end of the primary track, and on the first time point of each merging segment occurring after the start of the primary track. The segments discarded in this process corresponded to transient, abortive CCSs assembling in close vicinity to a longer-lived CCS.

2. Calculation of gap values

Gap intensities and positions were calculated by numerically fitting the 2-D Gaussian model used for detection at gap locations. Initializations for the fits were obtained by linear interpolation of the values preceding and following each gap. To avoid random localizations in noise at gaps without a trace signal, the fits were constrained to a radius of 2σ pixels (~200 nm).

3. Calculation of CCS fluorescence preceding and following the detected trajectories

CCS fluorescence prior to the first detected time point and following the last detected time point was estimated for a fixed number of “buffer” frames (typically 5), using sub-pixel localization of the 2-D Gaussian model described above. For each frame of these buffer readouts, the localization was initialized with the values of the signal at the first or last time point of the track, respectively. The localization was considered valid if the resulting position was within 2σ pixels (~200 nm) of the initialization; otherwise, the amplitude and background values were estimated by least squares using the position of the first and last detection, respectively.

4. Categorization and selection of valid CCS trajectories

Tracks were categorized as a function of whether they represented complete, partial (truncated at the beginning or end of the acquisition), or persistent (present throughout the entire acquisition) CCS trajectories, and as a function of gap length relative to the length of the track segments bounding each gap. Only trajectories for which the pre- and post-detection buffers could be fully calculated were considered complete. In order to avoid the inclusion of tracks containing sequences of gaps and frames resulting from the linking of independent short-lived events, tracks were classified based on gap properties in two sequential steps. First, tracks with gaps were considered valid if all gaps either consisted of a single frame, or were bounded by track segments of more than one frame. The maximum intensity distribution of these tracks was then calculated for a range of lifetime cohorts (typically [10-19], [20-39], [40-59], [60-79], [80-124], [125-150] s). In the second step, the remaining tracks with gaps were classified as valid if their maximum intensity was above the 2.5th percentile calculated for the respective lifetime cohort.

Next, tracks were further categorized as a function of the pre- and post-detection buffer intensities. Due to the high densities of CCSs observed in some cells and the limited search radius employed during the tracking step to avoid erroneous linking of independent CCS trajectories, some trajectories were truncated. These trajectories were filtered out based on high buffer intensities. Specifically, tracks were considered valid if the intensities of at least two consecutive frames in each buffer were below the detection threshold, and if the maximum intensity of each buffer was below the maximum intensity of the track.

A further criterion for validity was whether or not the CCSs corresponded to diffraction-limited structures. This was established by testing the residuals of the model fit performed during the detection step. For diffraction-limited objects, where the model is accurate, the residuals were expected to follow a normal distribution. The residuals of each fit were therefore tested for normality using the Anderson-Darling test. Trajectories that contained frames with non-normal residuals were excluded from further analysis.

5. Distinguishing gaps from sequential events

Using the u-track settings as described, CCSs forming in close spatial (~ 5 pixels) and temporal (≤ 3 frames) vicinity to the end of a preceding event were linked during the tracking process. Such trajectories were identified based on whether they contained gaps with intensities that were statistically indistinguishable from background. Gaps that occurred as a result of insufficient SNR contained residual intensity that remained statistically distinguishable from background. Furthermore, a spatial criterion was applied to corroborate erroneous linking. The individual positions corresponding to each of the two segments of a candidate trajectory were projected onto the line defined by the centroids of the two segments. If no overlap existed between the 95th and 5th percentiles of the resulting two distributions of positions, the trajectory was split into two independent trajectories.

Multi-channel (master/slave) detection and tracking

For multi-channel data, trajectories were obtained using the detections in the master channel containing the fluorescence of a fiducial marker for CCSs (i.e., clathrin or AP2). Fluorescence intensities in the secondary, or slave, channels were calculated through numerical fitting with the 2-D Gaussian model described for the detection step. The position in the slave channels was a free parameter in the fit in order to compensate both for CCS motion between the acquisitions of the individual channels, as well as for potential shifts due to chromatic aberration. The result of the fit was considered valid if the resulting position was within 3σ pixels (~ 300 nm) of the position in the master channel, and if the intensity was larger than the intensity estimated by least squares at the master position. Otherwise, the fit was considered failed due to insufficient signal, and least squares estimates of the amplitude and background using the position of the master signal were used instead. At the lowest SNR levels at which CCSs were detected (SNR of $\sim 4-5$), the localization accuracy is ~ 50 nm (determined theoretically using Cramér-Rao lower bounds). The median displacement between detections in the two channels was ~ 60 nm and a shift of ~ 30 nm due to chromatic aberration and/or misalignment between the two channels was estimated from the CCS localizations; this shift was consistent across all experiments.

Mapping of CCP trajectories independently tracked with $\mu 2$ -EGFP and enCLCa-RFP

The mapping of CCS trajectories independently detected using $\mu 2$ -EGFP and enCLCa-RFP was performed based on spatial proximity and temporal overlap of the signals. Trajectories were paired if the maximal distance between the trajectories was < 3 pixels (~ 300 nm), if there was at least 1 frame of overlap in time, and if the enCLCa-RFP trajectory started at most 5 frames before and ended at most 5 frames after the $\mu 2$ -EGFP trajectory. The last constraint was used to minimize bias from CCSs with insufficient $\mu 2$ -EGFP signal (due to the transient expression) in this analysis.

Calculation of lifetime distributions

Lifetime distributions were calculated from all tracks classified as valid during the post-processing described above. To avoid a potential bias from short tracks generated during the linking/gap closing steps but consisting of independent appearance of CCSs, tracks shorter than 5 frames were excluded from the analysis.

Due to the finite length of time-lapse acquisitions, there is an inherent bias in the lifetime measurement. Independent of the lifetime distribution, the probability of observing a specific lifetime is inversely proportional to that lifetime. Specifically, for a movie of n frames, the longest measurable track is $N = n - b_s - b_e$, where b_s and b_e are the length of the start and end buffer, respectively, in frames. The relative probability of observing a track with lifetime t is $(N - t + 1)/N$. The lifetime distributions were corrected for this factor, as previously described (Loerke et al., 2009).

Threshold for intensity-based decomposition of lifetime distributions

The time interval from the beginning of CCS assembly over which the maximum fluorescence intensity distribution was independent of lifetime was determined by a measure of similarity among these distributions across different lifetime cohorts. Statistical tests for similarity such as Kolmogorov-Smirnov or Anderson-Darling were not a sufficiently robust measure, likely due to heterogeneities in the long upper tails of the distributions. To avoid the influence of these tails, a measure of similarity based on the location of the peaks of the distributions was calculated. This was achieved by least-

squares fitting of a Gaussian function to the first mode of the distribution from each lifetime cohort (cohorts were generally chosen as [1-10], [11-15], [16-20], [21-40], [41-60], [61-120] s). For robustness, values larger than the mean of the Gaussian were excluded from the evaluation of the objective function. The distributions were classified as similar if the means obtained for the different cohorts were within the expected standard error, calculated from the parameters of Gaussian obtained for the first cohort (i.e., [0-10] s). The time interval for the threshold was chosen as the largest interval for which the distributions were similar by this measure. The threshold was chosen as the 95th percentile of the Gaussian fitted to the maximum intensity distribution for that interval, across all CCS trajectories.

Normalization of fluorescence intensities across data sets

To pool intensity values of CCS trajectories from n cells with different expression levels, a scaling factor a_i was determined for each cell i so that the cumulative distribution of maximum CCS intensities $F_i(x)$ in cell i was mapped to a reference distribution $F_{\text{ref}}(x)$ by minimizing $\int (c_i + (1 - c_i)F_i(x/a_i) - F_{\text{ref}}(x))^2 dx$. The constant c_i was used to estimate the amount of missing data between each distribution $F_i(x)$ and $F_{\text{ref}}(x)$; that is, between two cells the maximum intensity distribution of the lower-expressing cell is truncated with respect to the distribution of the higher-expressing cell due to a larger percentage of small, low-intensity objects falling below the detection threshold. The reference distribution $F_{\text{ref}}(x)$ was determined by first calculating the median distribution $F_{\text{med}}(x) = \text{median}(F_1(x), \dots, F_n(x))$ between the cumulative maximum intensity distributions of cells 1 to n . Subsequently, the reference distribution $F_{\text{ref}}(x)$ was selected as the distribution among $F_1(x), \dots, F_n(x)$ with the smallest integrated least-squares distance to $F_{\text{med}}(x)$.

Calculation of average intensities as a function of lifetime cohort

Average fluorescence intensities were calculated by interpolating all trajectories within a cohort to a length corresponding to the average lifetime of that cohort. Specifically, the intensities of trajectories in a cohort bounded by lifetimes $[t_0 \dots t_1]$ s were interpolated to the time vector bounded by $[0 \dots (t_0+t_1)/2]$ using cubic B-splines. This enabled the point-by-point averaging of the intensities. The time windows chosen for this averaging (typically in 20s intervals, e.g., [0-20], [20-40], [40-60], [60-80], [80-100], [100-120] s) were sufficiently small to avoid averaging artifacts.

Classification of Dyn2-positive and Dyn2-negative CCPs and calculation of the 'slave' significance threshold

CCP trajectories were classified as positive for a slave signal (e.g. Dyn2-EGFP) if this signal was significant (i.e., detectable independently of tdTomato-CLCa) for longer than a random association. The probability of random detection of a significant slave signal was calculated as follows: 1) A mask of the cell outline was calculated for each time-series by average-projecting all images after exclusion of CCP signals based on the CCP masks calculated as part of the detection process. This projection contained only background signal from inside and outside the cell, and its intensity distribution featured two distinguishable peaks. An intensity threshold was automatically selected as the minimum between these peaks and applied to the projection image to generate a cell mask. 2) The Gaussian PSF model was then fitted at 50000 random locations within the cell in the slave channel, and the significance of each fit was calculated with the t-test described for CCP detection. The fraction of significant fits yielded the probability p of random detection of an independently significant slave signal. For robustness, this probability was averaged across 10 frames evenly selected from each time-series. Trajectories were classified as slave signal-positive if the number of significant slave detections exceeded the number predicted by random association, which for each trajectory is given by the binomial distribution with parameters p and n , where n is the number of time points in the trajectory. Since the time points with significant slave detections in a trajectory were typically clustered, no explicit continuity constraint was enforced in this comparison.

The threshold to determine the significance of slave signals relative to background locations outside of CCPs was calculated using a similar procedure. The Gaussian PSF was fitted at 50000 random locations within the cell, but excluding locations within the CCP mask calculated during the detection step. This yielded a Gaussian-shaped distribution of background fluorescence. The slave significance threshold was selected as the 95th percentile of this distribution. For robustness, this threshold was also calculated across 10 frames evenly selected from each time-series and averaged. Photobleaching had a negligible effect on the value of this threshold and the probability p . To determine the significance of slave signals relative to this threshold at individual detections within a trajectory, a t-test analogous to the test described for detection was applied.

Curvature measurement by Epi:TIR fluorescence ratio

The epifluorescence to TIRF ratio was calculated for each trajectory as the maximum intensity detected in the epifluorescence channel divided by the maximum intensity detected in the TIRF channel. To normalize the intensities

between the two channels such that flat structures at the membrane yielded an Epi:TIR ratio of 1, a multiplicative correction factor was applied. This was calculated as the ratio between the mean intensity of the first detected frame of all trajectories in the TIRF channel relative to the mean intensity of the same set of detections in the epifluorescence channel, assuming that in the first frame of a trajectory CCSs are still flat.

Supplemental References

- Aguet, F., Geissbühler, S., Märki, I., Lasser, T., and Unser, M. (2009). Super-resolution orientation estimation and localization of fluorescent dipoles using 3-D steerable filters. *Opt. Express* *17*, 6829–6848.
- Antonescu, C.N., Danuser, G., and Schmid, S.L. (2010). Phosphatidic acid plays a regulatory role in clathrin-mediated endocytosis. *Mol. Biol. Cell* *21*, 2944–2952.
- Dedecker, P., Duwé, S., Neely, R.K., and Zhang, J. (2012). Localizer: fast, accurate, open-source, and modular software package for superresolution microscopy. *J. Biomed. Opt.* *17*, 126008.
- Doyon, J.B., Zeitler, B., Cheng, J., Cheng, A.T., Cherone, J.M., Santiago, Y., Lee, A.H., Vo, T.D., Doyon, Y., Miller, J.C., et al. (2011). Rapid and efficient clathrin-mediated endocytosis revealed in genome-edited mammalian cells. *Nat. Cell Biol.* *13*, 331–337.
- Henriques, R., Lelek, M., Fornasiero, E.F., Valtorta, F., Zimmer, C., and Mhlanga, M.M. (2010). QuickPALM: 3D real-time photoactivation nanoscopy image processing in ImageJ. *Nat. Methods* *7*, 339–340.
- Holden, S.J., Uphoff, S., and Kapanidis, A.N. (2011). DAOSTORM: an algorithm for high-density super-resolution microscopy. *Nat. Methods* *8*, 279–280.
- Jaqaman, K., Loerke, D., Mettlen, M., Kuwata, H., Grinstein, S., Schmid, S.L., and Danuser, G. (2008). Robust single-particle tracking in live-cell time-lapse sequences. *Nat. Methods* *5*, 695–702.
- Liu, Y.-W., Surka, M.C., Schroeter, T., Lukiyanchuk, V., and Schmid, S.L. (2008). Isoform and splice-variant specific functions of dynamin-2 revealed by analysis of conditional knock-out cells. *Mol. Biol. Cell* *19*, 5347–5359.
- Loerke, D., Mettlen, M., Yarar, D., Jaqaman, K., Jaqaman, H., Danuser, G., and Schmid, S.L. (2009). Cargo and dynamin regulate clathrin-coated pit maturation. *PLoS Biol.* *7*, e57.
- Motley, A.M., Berg, N., Taylor, M.J., Sahlender, D.A., Hirst, J., Owen, D.J., and Robinson, M.S. (2006). Functional analysis of AP-2 α and μ 2 subunits. *Mol. Biol. Cell* *17*, 5298–5308.
- Nunez, D., Antonescu, C., Mettlen, M., Liu, A., Schmid, S.L., Loerke, D., and Danuser, G. (2011). Hotspots Organize Clathrin-Mediated Endocytosis by Efficient Recruitment and Retention of Nucleating Resources. *Traffic* *12*, 1868–1878.
- Patterson, G., Davidson, M., Manley, S., and Lippincott-Schwartz, J. (2010). Superresolution imaging using single-molecule localization. *Annu Rev Phys Chem* *61*, 345–367.
- Sergé, A., Bertaux, N., Rigneault, H., and Marguet, D. (2008). Dynamic multiple-target tracing to probe spatiotemporal cartography of cell membranes. *Nat. Methods* *5*, 687–694.
- Subach, O.M., Gundorov, I.S., Yoshimura, M., Subach, F.V., Zhang, J., Grünwald, D., Souslova, E.A., Chudakov, D.M., and Verkhusha, V.V. (2008). Conversion of red fluorescent protein into a bright blue probe. *Chem. Biol.* *15*, 1116–1124.
- Wolter, S., Löschberger, A., Holm, T., Aufmkolk, S., Dabauvalle, M.-C., van de Linde, S., and Sauer, M. (2012). rapidSTORM: accurate, fast open-source software for localization microscopy. *Nat. Methods* *9*, 1040–1041.
- Yarar, D., Waterman-Storer, C.M., and Schmid, S.L. (2005). A dynamic actin cytoskeleton functions at multiple stages of clathrin-mediated endocytosis. *Mol. Biol. Cell* *16*, 964–975.